

The public reporting burden for this collection of information is estimated to average 1 hour per response, including the time for reviewing instructions, searching existing data sources, gathering and maintaining the data needed, and completing and reviewing the collection of information. Send comments regarding this burden estimate or any other aspect of this collection of information, including suggestions for reducing this burden, to Washington Headquarters Services, Directorate for Information Operations and Reports, 1215 Jefferson Davis Highway, Suite 1204, Arlington VA, 22202-4302. Respondents should be aware that notwithstanding any other provision of law, no person shall be subject to any penalty for failing to comply with a collection of information if it does not display a currently valid OMB control number.
PLEASE DO NOT RETURN YOUR FORM TO THE ABOVE ADDRESS.

1. REPORT DATE (DD-MM-YYYY) 07-03-2014	2. REPORT TYPE Final Report	3. DATES COVERED (From - To) 1-Jul-2009 - 30-Jun-2013
---	--------------------------------	--

4. TITLE AND SUBTITLE HIGH-STRAIN-RATE CONSTITUTIVE CHARACTERIZATION AND MODELING OF METAL MATRIX COMPOSITES	5a. CONTRACT NUMBER W911NF-09-1-0331
	5b. GRANT NUMBER
	5c. PROGRAM ELEMENT NUMBER 622618

6. AUTHORS K. Ravi-Chandar	5d. PROJECT NUMBER
	5e. TASK NUMBER
	5f. WORK UNIT NUMBER

7. PERFORMING ORGANIZATION NAMES AND ADDRESSES University of Texas at Austin 101 East 27th Street Suite 5.300 Austin, TX 78712 -1539	8. PERFORMING ORGANIZATION REPORT NUMBER
--	--

9. SPONSORING/MONITORING AGENCY NAME(S) AND ADDRESS (ES) U.S. Army Research Office P.O. Box 12211 Research Triangle Park, NC 27709-2211	10. SPONSOR/MONITOR'S ACRONYM(S) ARO
	11. SPONSOR/MONITOR'S REPORT NUMBER(S) 56104-EG.1

12. DISTRIBUTION AVAILABILITY STATEMENT Approved for Public Release; Distribution Unlimited
--

13. SUPPLEMENTARY NOTES The views, opinions and/or findings contained in this report are those of the author(s) and should not be construed as an official Department of the Army position, policy or decision, unless so designated by other documentation.

14. ABSTRACT The mechanical response of three different types of materials are examined: unidirectionally reinforced continuous fiber Al ₂ O ₃ /Al metal matrix composite, random fiber Saffil-fiber – aluminum matrix composite, and a satin-weave Nextel fiber reinforced aluminum matrix composite. Quasi-static tests and specially designed dynamic tests have been performed. For the split-Hopkinson bar test, in addition to the conventional measurements of the strain signals in the input and output bars, direct images of the deformation of the specimen were obtained using a Photron SA1 high speed video camera at 10 ² frame intervals. These measurements indicated that the deformation was localized.

15. SUBJECT TERMS metal matrix composites, dynamic response, failure mechanisms
--

16. SECURITY CLASSIFICATION OF:	17. LIMITATION OF ABSTRACT	15. NUMBER OF PAGES	19a. NAME OF RESPONSIBLE PERSON Krishnaswa Ravi-Chandar
a. REPORT UU	b. ABSTRACT UU	c. THIS PAGE UU	19b. TELEPHONE NUMBER 512-471-4213

Report Title

HIGH-STRAIN-RATE CONSTITUTIVE CHARACTERIZATION AND MODELING OF METAL MATRIX COMPOSITES

ABSTRACT

The mechanical response of three different types of materials are examined: unidirectionally reinforced continuous fiber Al₂O₃/Al metal matrix composite, random fiber Saffil-fiber – aluminum matrix composite, and a satin-weave Nextel fiber reinforced aluminum matrix composite. Quasi-static tests and specially designed dynamic tests have been performed. For the split-Hopkinson bar test, in addition to the conventional measurements of the strain signals in the input and output bars, direct images of the deformation of the specimen were obtained using a Photron SA1 high speed video camera at 10⁻⁷s time intervals. These measurements indicated that the deformation was localized due to the formation and propagation of a kink band. Based on an analysis of the power balance in the specimen, the rate of dissipation at the propagating kink band was estimated and used subsequently to determine that the dynamic dissipation was significantly greater than the quasi-static dissipation in the same material. The underlying reason was explored through a microscopic examination and attributed to increased fiber breakage under dynamic loading conditions. This report also documents some of the highlights of the material response of Saffil filled aluminum matrix composite and a Nextel satin weave reinforced aluminum matrix composite.

Enter List of papers submitted or published that acknowledge ARO support from the start of the project to the date of this printing. List the papers, including journal references, in the following categories:

(a) Papers published in peer-reviewed journals (N/A for none)

<u>Received</u>	<u>Paper</u>
-----------------	--------------

TOTAL:

Number of Papers published in peer-reviewed journals:

(b) Papers published in non-peer-reviewed journals (N/A for none)

<u>Received</u>	<u>Paper</u>
-----------------	--------------

TOTAL:

Number of Papers published in non peer-reviewed journals:

(c) Presentations

1. "High strain rate constitutive behavior of an Al/?-Al₂O₃ composite", Haitao Zhang and K. Ravi-Chandar, SEM 2009 Annual Conference, Albuquerque, NM, June 1-4, 2009.
2. "High-strain-rate constitutive behavior of an ?Al - Al₂O₃ composite", H. Zhang and K. Ravi-Chandar, 2009 International Mechanical Engineering Congress and Exposition, Lake Buena Vista, Florida, November 19, 2009.
3. "Dynamic response of an Al₂O₃/Al metal matrix composite", Haitao Zhang, K. Ravi-Chandar, Y.C. Chen, K. Cho, 2010 Materials Science and Technology Conference, Houston, TX, October 18, 2010
4. "Dynamic Properties and Failure of an Aluminum Matix Composite" 2011 MMC Materials Review – ARL, Aberdeen, MD, June 23, 2011

Number of Presentations: 4.00

Non Peer-Reviewed Conference Proceeding publications (other than abstracts):

Received Paper

TOTAL:

Number of Non Peer-Reviewed Conference Proceeding publications (other than abstracts):

Peer-Reviewed Conference Proceeding publications (other than abstracts):

Received Paper

TOTAL:

Number of Peer-Reviewed Conference Proceeding publications (other than abstracts):

(d) Manuscripts

Received Paper

TOTAL:

Number of Manuscripts:

Books

Received Paper

TOTAL:

Patents Submitted

Patents Awarded

Awards

Graduate Students

<u>NAME</u>	<u>PERCENT SUPPORTED</u>	Discipline
Andrew Gross	0.20	
FTE Equivalent:	0.20	
Total Number:	1	

Names of Post Doctorates

<u>NAME</u>	<u>PERCENT SUPPORTED</u>
Qunli Liu	0.20
FTE Equivalent:	0.20
Total Number:	1

Names of Faculty Supported

<u>NAME</u>	<u>PERCENT SUPPORTED</u>	National Academy Member
K. Ravi-Chandar	0.20	
FTE Equivalent:	0.20	
Total Number:	1	

Names of Under Graduate students supported

<u>NAME</u>	<u>PERCENT SUPPORTED</u>
FTE Equivalent:	
Total Number:	

Student Metrics

This section only applies to graduating undergraduates supported by this agreement in this reporting period

The number of undergraduates funded by this agreement who graduated during this period: 0.00

The number of undergraduates funded by this agreement who graduated during this period with a degree in science, mathematics, engineering, or technology fields:..... 0.00

The number of undergraduates funded by your agreement who graduated during this period and will continue to pursue a graduate or Ph.D. degree in science, mathematics, engineering, or technology fields:..... 0.00

Number of graduating undergraduates who achieved a 3.5 GPA to 4.0 (4.0 max scale):..... 0.00

Number of graduating undergraduates funded by a DoD funded Center of Excellence grant for Education, Research and Engineering:..... 0.00

The number of undergraduates funded by your agreement who graduated during this period and intend to work for the Department of Defense 0.00

The number of undergraduates funded by your agreement who graduated during this period and will receive scholarships or fellowships for further studies in science, mathematics, engineering or technology fields: 0.00

Names of Personnel receiving masters degrees

NAME

Total Number:

Names of personnel receiving PHDs

NAME

Total Number:

Names of other research staff

NAME

PERCENT SUPPORTED

FTE Equivalent:

Total Number:

Sub Contractors (DD882)

Inventions (DD882)

Scientific Progress

"See Attachment"

Technology Transfer

**HIGH-STRAIN-RATE CONSTITUTIVE
CHARACTERIZATION AND MODELING OF
METAL MATRIX COMPOSITES**

March 2014

**Final report to the
ARMY RESEARCH OFFICE
W911NF-09-1-0331
Krishnaswamy RAVI-CHANDAR**

Center for the Mechanics of Solids, Structures and Materials

THE UNIVERSITY OF TEXAS AT AUSTIN

TABLE OF CONTENTS

LIST OF FIGURES	iii
1. Introduction and Background	1
2. Dynamic Crushing of Unidirectionally Reinforced Metal-Matrix Composites	3
2.1. Quasi-Static Mechanical Response of Al ₂ O ₃ /Al Metal Matrix Composite	5
2.1.1. Stress-strain response	5
2.1.2. Deformation and failure mechanisms	7
2.2. Dynamic Mechanical Response of the Al ₂ O ₃ Metal Matrix Composite	7
2.2.1. Dynamic compression response of MMCs	8
2.2.2. Dynamic analysis of the crushing response	10
2.3. Summary of Unidirectionally Reinforced Al ₂ O ₃ Metal Matrix composite	12
3. Deformation and Flow of Saffil-Fiber Reinforced Metal-Matrix Composites	12
3.1. Quasi-Static Compression Response of Saffil-Fiber Filled MMC	13
3.2. Dynamic Compression Tests on Saffil-Fiber Filled MMC	14
4. Behavior of Satin-Wave Nextel Fiber – MMC (DF19)	16
5. Summary and Conclusions	17
REFERENCES	19

LIST OF FIGURES

Figure 1	Microstructure of the Nextel 610 Al composite. (a) Transverse section indicating matrix rich layers and a high magnification of the transverse section indicating the peanut shape cross-section: $\sim 16 \times 8 \mu\text{m}$; (b) Axial section indicating the nominal orientation of the unidirectional fibers and some misaligned fibers. The red solid line is the nominal fiber direction, while the red dashed lines are parallel to the fiber direction and indicate the degree of misalignment.	21
Figure 2	(a) True stress vs true strain variation for the elastic portion of the response. (b) Nominal stress vs nominal strain response of the specimen that covers initiation of the kink band as well as the steady state crushing of the specimen.	22
Figure 3	(a) Photograph of a specimen that was unloaded just past the initiation of the kink band localization. (b) Specimen that was crushed through nearly half of its initial length; petaling type of failure is observed.	23
Figure 4	An axial section of the specimen interrupted just past the initiation of the kink band is shown. The red dashed lines indicate the orientation of the kink band, which is $\sim 15^\circ$ with respect to the loading axis. High magnification images of the regions at the band ends indicate bending and fracture of the fibers. At the central region, the intersection of bands oriented along two equivalent planes result in significant fragmentation of the fibers.	23
Figure 5	Time variation of the reflected signal in the input bar converted the nominal strain rate in the specimen (blue line) and the transmitted signal in the output bar converted to the stress in the specimen (red line). The gray vertical lines indicate times at which high speed video images were recorded. Labels (a) through (e) identify the times corresponding to times for which images are shown in Figure 6.	24
Figure 6	Selected frames from the high speed video sequence of one test indicating the uniform strain development up to frame (c) and kink band propagation from stage (d).	24
Figure 7	Variation of the kink initiation and propagation stress with loading rate.	25
Figure 8	The time variation of the position of the left edge of the specimen and the position of the kink band (labeled damage front) with reference to the right edge of the specimen.	25
Figure 9	Geometry of the specimen indicating the nonuniform strain distribution. The input and output bars are in contact with the specimen at $x = 0$ and $x = l$, respectively. The kink band is at $x = s(t)$..	26
Figure 10	Time variation of the dissipation rate, \dot{D} (solid red line), and the stress in the specimen (blue dashed line).	26

Figure 11	Variation of the dissipation rate with the loading rate.	27
Figure 12	Loading rate dependence of dissipation during kink band propagation.	27
Figure 13	Axial sections of two specimens, at loading rates $\dot{\sigma} = 24.6$ and $\dot{\sigma} = 54.9$ MPa/ μ s respectively, in the top and bottom images, indicating the kink band progression. The red dashed lines indicate the orientation of the kink band, which is $\sim 15^\circ$ with respect to the loading axis, similar to that in the quasi-static kink propagation. High magnification images of the regions at the band ends indicate bending and fracture of the fibers. The main difference from quasi-static band propagation appears to be in the increased number of fragments in the dynamic experiments.	28
Figure 14	Quasi-static compression response of Saffil fiber aluminum matrix composites. Matrix response indicates a very small initial yield strength.	29
Figure 15	Elastic modulus of Saffil fiber aluminum matrix composites, obtained from the unloading segments in Figure 1. The estimate from the rule of mixtures is indicated by the open circular symbols.	29
Figure 16	Shear localization and failure response of Saffil fiber aluminum matrix composites (15% Saffil, Al2%Cu Matrix). Cracks have appeared, typically in the boundary of the shear band	30
Figure 17	Close up view of the shear localization in Figure 16. (15% Saffil)	30
Figure 18	Scanning electron micrograph of the 15% Saffil in the region of the shear band. Matrix damage and microcracks appear over a much smaller portion of the shear band (over 10 μ m near one boundary).	31
Figure 19	Dashed lines show specimen response after inhomogenous deformation begins. P03 specimens were not recorded with high speed imaging so the boundary between material and structural response is unknown.	32
Figure 20	The dependency of load carrying response in the damaging regime on strain rate is large. The separation between the two blue curves is caused from the interaction between the specimen and loading frame during specimen fracture.	33
Figure 21	Optical micrograph of 30% Saffil composite after dynamic compression. Damage is visible outside the dominant band.	34
Figure 22	Optical micrograph of the satin-weave Nextel – Aluminum matrix composite.	35
Figure 23	Tensile stress-strain response of DF-19 (0/90 satin weave Nextel-aluminum matrix composite). The only material to exhibit a ductile response was tested in the matrix dominant direction (perpendicular to the fibers).	36
Figure 24	Fracture surface of a broken DF-19 satin-weave (0/90) Nextel-fiber aluminum matrix composite. The complete infiltration of the metal	36

inside the fiber tows can be seen in this micrograph.

Figure 25	Quasi-static compression response of Nextel fiber aluminum matrix DF-19 composites. Matrix response indicates a very small yield strength as shown in Figure 1.	37
Figure 26	Shear localization and kinks in the fiber. Nextel-aluminum matrix DF-19 specimen under compression. The shear band makes an angle of 54° with respect to the loading axis.	38
Figure 27	Close up view of the shear localization and kinks in Figure 26.	38
Figure 28	Scanning electron microscope image of the boundary of the shear band indicating large fiber rotation, fiber fracture and matrix cracking.	39

1. Introduction and Background

Metal matrix composites (MMCs) have been identified as a class of attractive materials for numerous applications due to their excellent mechanical and physical properties (high specific stiffness and strength, low weight, and wear-resistance, etc.), ease of manufacture, and low cost of production. In military or aerospace structures, MMCs are expected to be used as energy absorbing structures or protective coatings which are often subject to blast loading or dynamic impact [Chin 1999]. In these applications, understanding and modeling the strain rate-dependent, constitutive and failure behavior of MMCs is important. An MMC usually contains at least two distinct phases: hard ceramic particles or continuous fibers that serves as the reinforcement phase and a metal as the matrix phase. The ceramic particles or fibers provide high stiffness and strength to the composite while the metal matrix provides a compliant support for the reinforcement and overall ductility. MMCs are typically produced by combining two pre-existing constituents, through processes such as powder metallurgy and squeeze-infiltration. Over the past decades, processing of MMCs has seen great advances, presenting a variety of novel composite systems. This has triggered an extensive study on MMCs and there exists a large literature on this subject. However, most of the work to date has focused on specific commercial or near-commercial materials [Lloyd 1994, Ibrahim et al. 1991] without providing fundamental understanding of processing effects and links between microstructure and thermo-mechanical properties. Much work remains to be done before required properties can be systematically achieved via microstructural design. Such demand is imperative for MMCs which are to be used in harsh environments of impact or blast loading where the demands on property data and design guidelines are great, but currently not met. An MMC usually exhibits improved aggregate mechanical properties when compared to either the metallic matrix phase or the reinforcing component. Property improvements of MMCs have been sought successfully in stiffness and strength by increasing the volume fraction of reinforcement. However, properties such as ductility and toughness usually fall with the increase of reinforcement [Zhang et al. 2008, Kiser et al. 1996]. Improvement of ductility and toughness, especially those under dynamic loading, through microstructure optimization is of highest interest for applications of MMCs in energy absorbing structures or protective coatings. Even though most MMCs studied to date are aluminum matrix composites, magnesium and its alloys have also been considered to be good candidates for the matrix of MMCs as light structural metals with mechanical properties

comparable to aluminum alloys. In recent years, the world has witnessed a dramatic growth of the magnesium industry which in turn advances the processing and applications of magnesium matrix composites. Despite the many research efforts on mechanical properties of magnesium and magnesium matrix composites at quasi-static strain rates [Lloyd 1994, Luo 1995, Saravanan 2000], the research on mechanical properties of these materials at elevated strain rates is still in its infancy compared to their fast growth of applications.

Modeling work with intent to predict the thermo-mechanical constitutive behavior of MMCs has been carried out over the past decades and various models have been developed. In general, these models can be grouped into two classes: analytical models that are based on continuum micromechanics or dislocation plasticity, and numerical models that are based on finite element method (FEM) or other computation methods. Law of mixtures [Voigt 1889], shear lag [Cox 1952], laminated plate [Jones 1975], Eshelby's [1957] and variational principle [Hershey 1954] models belong to the first group, which generally provides fundamental understanding and qualitative predictions of the thermo-mechanical properties of MMCs. Strengthening from simple characteristics of the microstructure of composites, such as reinforcement volume fraction and simple shapes, can be captured by these models. Numerical models, on the other hand, provide an approach to study the influence of more realistic geometric and spatial distribution of the phases (i.e. complicated reinforcement shape, clustering, and connectivity) in MMCs by means of simulating the deformation and failure of a representative volume element (RVE) of the microstructure. Unit-cell models with one or more reinforcements, which represent a periodic arrangement of the microstructure, are typical examples of this group models. The phenomenal growth of numerical models is attributed to the increasing power of digital computers and to the advances in numerical simulation techniques. The effect of damage, which is hard to describe analytically, has also been taken into account in these models successfully [Zhang et al. 2006]. Recently, multiscale finite element modeling has also provided a new approach to capture different physical mechanisms (such as micromechanics and damage evolution) in deformation of MMCs at various length and time scales [Totry et al. 2008]. This opens a new door for simulations of the mechanical responses of MMC materials or structures under extreme conditions.

The primary objective of this research project was to understand the influence of microstructure on the high-strain-rate behavior and dynamic failure of fiber/particulate reinforced

metal matrix composites. Factors affecting the MMC properties include reinforcement volume fraction, reinforcement size, reinforcement shape, and matrix-reinforcement bonding property. Effects from material processing and preparation will also be considered. Special efforts were made to understand the effect of matrix-reinforcement interfacial property and failure on the high-strain-rate response of MMCs. This research is expected to provide guidelines for material designers and structural engineers in production and applications of a new generation of lightweight energy absorbing materials.

2. Dynamic Crushing of Unidirectionally Reinforced Metal-Matrix Composites

Metal matrix composites (MMCs) are materials that have high specific strength and specific modulus (per unit mass) in comparison to conventional metals and alloys. Unlike polymer matrix composites that have a very high anisotropy of properties in the fiber direction vs the transverse direction, and quite poor transverse properties, MMCs are only mildly anisotropic and exhibit significant enhancement in the transverse properties as well. A survey of the mechanical properties and applications of Alumina reinforced aluminum alloy can be found in an overview article by Deve and McCullough (1985). The mechanical response of continuous fiber reinforced metal matrix composites have been investigated under different loading conditions by many investigators. For example, Shetty and Chou (1985) examined the tension and compression properties of continuous alumina and tungsten fiber reinforced aluminum composites. They found a bilinear stress-strain response both under tension; furthermore, kinking mode of failure was observed in the unidirectional composite under compression. Since the strength under compression is quite sensitive to the fiber misalignment and to end conditions, special compression fixtures were used to explore the variability. It was determined that the height to width ratio of about 3 resulted in the maximum recorded compression strength. The impact response has also been explored through various experiments, but primarily using the split-Hopkinson or Kolsky bar apparatus. Lee et al. (2000) used a split-Hopkinson pressure bar apparatus to determine the compressive stress-strain response of carbon fiber reinforced Al 7075 composite, with a very low volume fraction (~10%) of fibers. The analysis of the experimental data was performed assuming homogeneous stress and strain state within the specimen, and

significant anisotropy of material response was observed. The transverse strength of a unidirectional carbon fiber reinforced cast aluminum alloy was explored by Dai and Bai, (1998). Strain rates on the order of 10^3 s^{-1} were achieved in these tests; it was determined that the transverse shear strengths are significantly lower than that of the matrix alone, mainly due to the nucleation, extension and coalescence of defects. The compressive response of an alumina reinforced aluminum matrix composite under dynamic loading is the focus of this article.

The compressive strength of fiber reinforced materials has been of long standing interest. This is particularly true for unidirectionally reinforced polymer composites, where due to the onset of fiber buckling influenced significantly by the fiber misalignment, the compressive strength is typically significantly low in comparison to the tensile strength. In contrast, composites with a ceramic reinforcement and metal matrix exhibit significantly higher compressive strength than tensile strength (see for example, Deve, 1997). However, their failure is still triggered by the same buckling instabilities as in the polymer matrix composites. Rosen (1965) identified that a global elastic buckling of the unidirectional fibers would limit the compressive strength; based on an analysis in which the matrix effect was incorporated through a beam-on-elastic foundation model, Rosen determined that the compressive strength would be equal to $G/(1-\nu_m)$, where G is the shear modulus and ν_m is the fiber volume fraction. However, Argon (1972) recognized that the buckling occurred at a local level in the form of a kink because of fiber misalignments, and this was influenced by the plastic response of the matrix. Based on a simple analysis of the effect of misalignments of microscale kinks, Argon estimated that the compressive strength should be σ_m/θ , where σ_m is the matrix yield strength and θ is the largest local fiber misalignment. Budiansky and Fleck (1993) extended the Argon model incorporating the strain hardening behavior of the matrix. In very carefully controlled experiments, Kyriakides et al (1995) and Vogler and Kyriakides (1999) explored the geometry and the initiation and growth of the kink band as it forms across a finite width specimen of AS4/PEEK composite. Initially, the bands formed at 15° over a narrow width on the order of about 250 fiber diameters. Subsequently, they found that the kink band broadened at a steady load, by bending and breaking of fiber in the vicinity of the inclined bands. Argon (2000) estimated the band angle by a simple estimate based on the bending strain required for attaining fiber fracture.

This section is organized as follows: a brief description of the material – alumina fiber reinforced aluminum matrix composite – and its quasi-static response is provided in Section 2.1. This is followed by a description of the experiments performed to investigate the dynamic crushing response of the material in Section 2.2. These experiments are performed in a standard split-Hopkinson pressure bar apparatus; however, it is shown that nonuniformity of the strain field is unavoidable, thereby necessitating new procedures for analysis and interpretation of the data that are considered in Section 2.3.

2.1. Quasi-Static Mechanical Response of Al₂O₃/Al Metal Matrix Composite

The focus of this section is on the compressive strength of Nextel 610 alumina fiber reinforced aluminum matrix composites. The microstructure of the composite is shown in Figure 1, where the transverse and axial plane sectional views as well as a high magnification view of the material microstructure are shown. The fibers are α -Al₂O₃ have a peanut shape cross-section with dimensions $\sim 16 \times 8 \mu\text{m}$ as shown in Figure 1c. The fiber volume fraction is roughly 40 to 50% and the density of the α -Al₂O₃/Al composite is $\sim 3.2 \text{ kg/m}^3$. The microstructure shows that the matrix has infiltrated the gaps between the fibers completely. The peanut shaped fiber is dispersed uniformly with respect to its axial orientation, but there appear matrix rich layers as indicated in Figure 1a. Recalling from the previous section that misalignments contribute to a decrease in compressive strength, it should be noted that the axial section in Figure 1b indicates misalignment of many fibers; the nominal orientation of the unidirectional fiber is indicated by the solid (red) line, while a few of the misaligned fibers are identified by the dashed (red) line. It should be recognized that there is possible misalignment in the other orientation (axial-short transverse), and this shown up in Figure 1b as fibers that terminate abruptly. The estimated maximum misalignment is about 5° . Both the fiber misalignment and matrix rich regions will drive the compressive strength of the composite towards the matrix strength.

2.1.1. Stress-strain response

As described earlier, it is well recognized that end effects contribute significantly to the onset of the kink band in unidirectional composites. The ASTM D3410-03 describes the use of end tabs and confinement of the ends inside a confining fixture in order to prevent failure from the ends of

the specimen and to promote failure within the gage section of the specimen. However, such end fixtures are difficult to implement under dynamic loading conditions and most dynamic experiments on metal matrix composites (Dai and Bai, 1998; Yadav et al. 1995; Lee et al. 2000) have not used compression end tabs; we will also not use end tabs in the work presented here. The net result is that the stress at the nucleation of the kink band cannot be obtained in these experiments, but the stress required for the growth of the kink band localization can be obtained directly from the measurements.

The quasi-static response was evaluated by fabricating specimens with a diameter of 8 mm and length of 16 mm. The specimen was loaded in uniaxial compression oriented along the fiber direction using an Instron test machine at a nominal strain rate of 10^{-4} s^{-1} . The local strain was monitored using Digital Image Correlation (DIC; Chu et al., 1985). The ends of the specimen were loaded in compression through a tool steel plate in order to prevent localized indentation into the specimen or the loading platens of the Instron. A typical stress vs strain response of the specimen is shown in Figure 2. The early response shown in Figure 2a (to strain levels of about 0.006%) in terms of the true stress vs true strain, is linear and elastic and the deformation was found to be uniform along the entire length of the specimen. The elastic modulus obtained from this measurement is about 195 GPa, and falls within the bounds estimated from a simple rule of mixtures formula for the $\text{Al}_2\text{O}_3/\text{Al}$ composite (190 -220 GPa). At the point corresponding to the peak load, localized damage in the form of a kink band initiates at one end of the specimen. The stress level at which this occurs varies in the range from 0.975 to 1.2 GPa, and is in the lower end of the range of compression strengths reported by Shetty and Chou (1985), and is clearly influenced by the absence of end constraints. Upon onset of this instability, the nominal stress in the specimen drops rapidly to about 400 MPa in an uncontrolled manner; the nominal strain in the specimen jumps to about 2.5% because of the recovery of the displacement in the load cell; however, the true strain in the regions outside the kink band dropped to ~ 0.0025 corresponding to the 400 MPa stress. For one specimen, the test was stopped at this point in order to explore the nature of the localization – a kink band; this can be seen in Figure 3a. Continued displacement of the cross-head beyond this point results in gradual progression of the kink band along the length of the specimen; it should be noted that since the stress in the region outside the kink band is quite low, around 400 MPa, in comparison to the stress for onset of kink bands, no further nucleation of kink bands can

occur in the specimen. A final image of the specimen is shown in Figure 3b; a video of the progression of crushing will be published in the archival literature, where the failure resembling the opening of a petal can be seen. The nominal stress remains nearly constant at about 400 MPa as the crushing envelops the entire specimen as shown in Figure 2b. This stress level is significantly greater than the flow strength of the aluminum matrix and must be influenced by the bending and fracture of the fibers, and the cracking of the matrix.

2.1.2. Deformation and failure mechanisms

The nature of the kink band was examined through microscopy of the failed specimens. The specimen was sectioned parallel to the axis of the cylinder, polished using standard metallographic preparation procedures, and images at high resolution in an optical microscope. The images shown in Figure 4 indicate the nature of the kink band. As is typical of unidirectionally reinforced composites, a kink band forms at an angle with respect to the loading axis; there is significant three dimensionality to the band formation early on as can be observed from the top portions of the specimen in Figure 3, but once a steady growth is established the band is approximately at an angle of 15° with respect to the loading axis as indicated by the two red dashed lines in Figure 4. High magnification views of the boundaries of the kink band indicate significant rotation of the fibers, facilitated by the nearly periodic fracture of the Al₂O₃ fibers.

2.2. Dynamic Mechanical Response of the Al₂O₃/Al Metal Matrix Composite

We examine the dynamic response of the MMC using a split-Hopkinson pressure bar (SHPB) apparatus. This method is rather well-established and it is really not necessary to provide any explanation of either the technique or the data analysis procedure, if the primary purpose is to explore the strain-rate dependence of the material response. If sufficient care is taken in sizing the specimen to ensure that inertial effects are minimized and that uniformity of stress and strain are established, then the conventional interpretation of the signals measured in the input and output bars can be used to determine the dynamic stress and strain in the specimen. However, while homogeneity of stress can be inferred directly from the measured strain signals, establishment of strain homogeneity requires the use of a direct strain measuring methods, such as high speed

photography. In cases where strains are not homogeneous over the length of the specimen, additional considerations are required in order to interpret the strain signals measured in the input and output bars in terms of the response of the material. These considerations turn out to be quite significant in the investigation of the MMCs where, as observed in the quasi-static tests, the kink band localization occurs at one of the ends and then propagates through the rest of the specimen, rendering the strain nonuniform along the specimen and thereby invalidating the usual analysis used to interpret the split-Hopkinson pressure bar results. In this section, we first describe the results of the dynamic compression experiments; this is then followed by an interpretation of the data in terms of the propagation of the crushing front in the MMC where a measure of the rate-dependent dissipation in the process of kink band propagation is obtained.

2.2.1. Dynamic compression response of MMCs

The incident and transmitted bars of the SHPB apparatus were made of 12.7 mm diameter maraging steel. A 150 mm long striker bar was used to generate the stress pulses; a soft Cu101 pulse shaper was used to eliminate high frequencies in the input pulse. Nominal strain rates in the range of 3000 s^{-1} are achieved in this apparatus. While the strain in the incident and transmitted bars were monitored with strain gages and recorded on an oscilloscope, additional information was obtained by using a Photron SA1 high speed video camera; these images were recorded at $10 \mu\text{s}$ time intervals, with an exposure time of $3.5 \mu\text{s}$. The specimens used for the SHPB experiments were of diameter 8 mm and length 5 mm.

The result from a typical experiment is shown in Figure 5. The reflected and transmitted signals are shown in Figure 5a; as in a typical SHPB test, the reflected signal is converted to the nominal strain rate $\dot{\epsilon} = -2C_b \epsilon_R / L_s$ where C_b is the bar wave speed of the input bar L_s is the length of the specimen, and ϵ_R is the reflected strain signal; this is indicated by the blue line in Figure 5. Similarly, the transmitted signal is converted to indicate the stress in the specimen $\sigma = A_b E_b \epsilon_T / A_s$ where E_b is the modulus of elasticity of the output bar, A_b, A_s are the areas of the output bar and specimen, respectively, and ϵ_T is the transmitted strain signal; this estimated stress shown by the red line in Figure 5. It was verified that indeed that $\epsilon_T = \epsilon_I + \epsilon_R$, (where ϵ_I is the incident strain pulse) assuring that the force on either side of the specimen was equal.

However, this is not sufficient to interpret the reflected signal in terms of the strain rate in the specimen; uniformity of the strain in the specimen must be examined. Frames from the high-speed video record, at selected points labeled (a) through (e) in Figure 5 are shown in Figure 6. A complete video file of the test will be available as Supplementary Material to an archival article. From the video images and the input and output bar signals, the following are evident:

- Between frames (a) and (c), the deformation in the bar appears to be uniform. This is the range in which the SHPB should provide nearly constant strain rate deformation and the reflected strain signal in Figure 5 supports this assertion.
- Beyond the point (c) the deformation localizes in the form of a kink band at the left end corresponding to the image (d). Corresponding to the onset of this kink band formation, the stress in the specimen drops from a peak value of about 1.33 GPa to a value of around 0.5 GPa. Associated with this drop in the ability of the specimen to support stress, the incident wave encounters lower impedance and hence the magnitude of the reflected wave increases significantly; in fact, the reflected strain signal could no longer be interpreted in terms of the specimen strain. The magnitude of the peak depends on the rate of loading; this variation is shown in Figure 7.
- Subsequently, the kink band continues to move into the specimen as seen in image (e). During the growth of the kink band from (d) to (e), the stress remains constant, just as in the quasi-static experiments, but at 0.5 GPa. This is the propagation stress, σ_p , and is found directly from the measurement of the transmitted signal in the output bar. The magnitude of the stress at which steady propagation of the kink band (damage) occurs appears to be less dependent upon the rate of loading and hovers around 0.5 GPa as shown in Figure 7.

It is essential to note that during this stage, the reflected strain signal cannot be interpreted as the strain rate in the specimen because, clearly, the specimen exhibits nonuniform strain over its length, with the right side remaining at the strain corresponding to an uncrushed specimen at a stress level of 0.5 GPa, while the kink band that initiated at the left end continues to move to the right. It is also clear that the kink band moves while the specimen remains at a constant stress level of 0.5 GPa; in order to explore the response further, we examine the speed of movement of the kink band. This is accomplished by tracking the position of the input and output bars where they contact the specimen as well as the location of the kink band as identified visually from the high speed

images. This is shown in Figure 8, where the time variation of the position of the left edge and the kink band relative to the right edge are shown. The kink band (or damage front) moves into the specimen at a speed of about 80 m/s; this speed depends on the impact generated from the input bar. We now turn to the analysis of the crushing response by considering the wave propagation in a little more detail.

2.2.2. *Dynamic analysis of the crushing response*

From the direct measurements, two things are clear: first, during steady-state progression of the kink band, the stress in the specimen is uniform at the propagation stress $\sigma_p \sim 0.5$ GPa, far below the stress required for nucleation of the kink band. Second, the strain is nonuniform in the specimen with two distinct sections – an undamaged section of the specimen that is strained elastically to $\varepsilon = \sigma_p / E \sim 0.0026$, and a fully damaged section whose homogenized strain is difficult to determine directly from the measurements; however, the lengths of both sections can be obtained from the experimental data as indicated in Figure 8. In order to analyze the results further, we need to consider wave propagation in the specimen.

Consider one-dimensional wave propagation in a material with an arbitrary nonlinear material behavior; for the purpose of the analysis described here, it is not necessary to assume a form of the stress-strain behavior. Consider the instant in time when the kink band is at a Lagrangian location $x = s(t)$, with the crushed material occupying $0 < x < s(t)$ and the undamaged material occupying $s(t) < x < l$ as indicated in Figure 9. We now develop a simple method of estimating the rate of dissipation that can be obtained using the standard measurements generated in a SHPB experiment. The power balance equation can be written as

$$\dot{W}_L - \dot{W}_R = \dot{W}_d + \dot{W}_u + \dot{K} + \dot{D}$$

where \dot{W}_L, \dot{W}_R are the power input at the left and right edges of the specimen, respectively, \dot{W}_d, \dot{W}_u are the rate of change of stress work in the damaged and undamaged sections respectively, \dot{K} is the change of kinetic energy, and \dot{D} is the rate of dissipation in the zone where undamaged material gets converted to damaged material. The power flow at the interface between the input bar and the specimen is $\dot{W}_L = \sigma_L v_L$, where $\sigma_L = E(\varepsilon_l - \varepsilon_r)$, $v_L = C(\varepsilon_l + \varepsilon_r)$ are obtained directly

from the strain measurements in the input bar. Similarly, $\dot{W}_R = \sigma_R v_R$ with $\sigma_R = E \varepsilon_T$, $v_R = C \varepsilon_T$ and is obtained from the strain measurement in the output bar. Substituting these into the power balance and rearranging, we obtain an expression for the dissipation rate:

$$\dot{D} = (\sigma_L v_L - \sigma_R v_R) - \frac{d}{dt} \int_{s^+}^l W_i(x) dx - \frac{d}{dt} \int_0^{s^-} W_c(x) dx - \dot{K}$$

where s^+, s^- indicate locations just to the left and right of the kink band. To make further progress, we must estimate the time rate of change in stress work density and the kinetic energy; however, from the high speed images, it is clear that the damaged region does not consume further energy since it simply moves away along the petals. Therefore, we assume that \dot{W}_d, \dot{W}_u and \dot{K} are negligible; this assumption can be further justified by a simple consideration: the undamaged region is strained only to about 0.0025, and after passing through the kink band, petals away and releases the energy corresponding to this strain resulting in a rather small value for \dot{W}_d, \dot{W}_u in comparison to the other terms. In cases where the stress work density changes are not negligible, additional measurements (or a model of the damage process) would be necessary. Similar considerations apply for the rate of change in the kinetic energy. Therefore the rate of dissipation is easily estimated from the measurements in the SHPB.

Using the above procedure, we convert the measured signals in the input and output bars to the dissipation rate and stress in the specimen; a typical result is shown in Figure 10. From this result, it can be seen that the dissipation rate can be approximated as a constant indicated by the dashed red line during steady propagation of the kink band. Since the strain rate is not an appropriate measure of the loading condition, we identify the loading rate with the rate of increase of the stress in the specimen, $\dot{\sigma}$; the steady dissipation rate is plotted in Figure 11 as a function of the stress rate from a collection of kink band propagation experiments. Integrating the estimate of the dissipation rate with time, one obtains the total dissipation in the process of the kink band growth; this is shown in Figure 12, in comparison with the dynamic plastic dissipation at comparable nominal strain for an Al 6061-T6.

The origins of the loading rate dependence of the dissipation during kink band propagation can be identified by considering the nature of the dynamic kink band; it is not expected to be in the intrinsic strain-rate dependent material behavior since the strain rates are not high enough.

The nature of the kink band was examined through microscopy as in the case of quasi-static tests described in Section 2.1.2. The failed specimens were sectioned parallel to the axis of the cylinder, polished using standard metallographic preparation procedures, and imaged at high resolution in an optical microscope (see Figure 13). Similar to the quasi-static response, the kink band forms at an angle of approximately 15° with respect to the loading axis as indicated by the two red dashed lines in Figure 13. High magnification views of the boundaries of the kink band indicate significant rotation of the fibers, facilitated by the nearly periodic fracture of the Al_2O_3 fibers. The fragmentation of the fibers under dynamic loading conditions appears to be at a smaller length than in the quasi-static kink band propagation; this must play a main role in the increased dissipation observed.

2.3. Summary of Response of Unidirectionally Reinforced Al_2O_3 Metal Matrix Composite

The dynamic response of unidirectionally reinforced continuous fiber $\text{Al}_2\text{O}_3/\text{Al}$ metal matrix composite has been explored using a standard split-Hopkinson pressure bar apparatus. In addition to the conventional measurements of the strain signals in the input and output bars, direct images of the deformation of the specimen were obtained using a Phtron SA1 high speed video camera at $10 \mu\text{s}$ time intervals. These measurements indicated that while the stress on either side of the specimen attained the same value assuring stress uniformity along the length of the specimen, the deformation was localized due to the formation and propagation of a kink band. Based on an analysis of the power balance in the specimen, the rate of dissipation at the propagating kink band was estimated and used subsequently to determine that the dynamic dissipation was significantly greater than the quasi-static dissipation in the same material. The underlying reason was explored through a microscopic examination and attributed to increased fiber breakage under dynamic loading conditions.

3. Deformation and Flow in Saffil-Fiber Reinforced Metal-Matrix Composites

Saffil-fiber filled metal matrix composite specimens were supplied by the Army Research Laboratory, Aberdeen Proving Grounds for performing quasi-static compression, quasi-static tension, and dynamic compression tests. The matrix in these composites is an Al-2%Cu alloy; matrix specimens were also supplied in order to extract the matrix properties. The specimens had

fiber volume fractions of 4, 15 and 30% to cover a range of fiber fractions. Over two hundred tests have been performed and analyzed; here, we present only the highlights.

3.1. Quasi-static Compression Response of Saffil-Fiber Filled MMC

These tests were performed on specimens with a rectangular cross-section (9.50×7.73 mm) at a strain rate in the range of 5.2×10^{-4} 1/s. Since the elastic range was extremely small, the specimens were unloaded after a strain level of 5 to 6 percent and the unloading slope was used to identify the elastic modulus; the unloading strain rate was also lowered by an order of magnitude in order to facilitate data collection. In order to eliminate the effects of the loading train compliance on estimation of the specimen strain, Digital Image Correlation (DIC) method was used to measure the strains; the load cell data was collected to estimate the stresses.

The quasi-static compression responses from 18 tests are shown in Figure 14. Four of these are from the matrix material (specimens labeled AICu PLATE 01 and 02). It is clear that the matrix has very low yield strength; this is due to the fact that the matrix is mostly aluminum, with 2% copper and no strengthening mechanisms have been introduced by control either of grain size or of the heat-treatment. Significant flow of the material occurs at stress levels of just above 25 MPa. However, due to dislocation multiplication and grain boundaries, the matrix does exhibit significant strain hardening. After a strain level of about 7% an unloading – loading cycle was performed to estimate the elastic modulus of the material; this value of the modulus was estimated to be 70 MPa. The remaining fourteen tests were on Saffil filled composites, with the volume of the Saffil maintained at 4%, 15% and 30%. For the 15% and 30% Saffil composites, two different orientations – normal and transverse to the plate directions – were tested. These results fall into three clusters, one for each volume fraction of the Saffil. With increasing volume fraction of Saffil, the initial slope of the stress-strain response – still dominated by matrix plasticity – increases. The elastic moduli of these composites were once again determined by the response during unloading. The variation of the modulus of elasticity with volume fraction of Saffil is shown in Figure 15, along with a comparison to the estimate from the rule of mixtures. While the rule of mixtures gives a reasonable estimate of the elastic modulus at the lower volume fractions, the deviation at the 30% Saffil is large; two possible sources will be examined. First, there appear to be local fluctuations in the fiber distribution that could result in the lower

observed modulus. Second, as will be demonstrated through failure analysis later, the fibers get broken to small pieces during large plastic deformations; if the fibers break into small enough pieces, their stiffening effect could be reduced. We are examining both possibilities to explain the difference between the measured elastic modulus and the rule of mixtures estimate. It is interesting that even though the matrix is soft, the incorporation of the fibers increases the flow stress significantly; we need to explore the nonlinear composite response using unit cell simulations.

While most of the specimens were unloaded in order to estimate the elastic modulus, some of the specimens were loaded to failure. At the 15% and 30% Saffil concentration, such failure occurred abruptly, with a sudden load drop. The failure in these composites is due to a matrix-dominated shear localization. This is illustrated in Figure 16, where an optical microscope image of a polished section is shown. The two red lines indicate the boundaries of the shear band and demonstrate that the shear band occurs at an angle of 45° with respect to the loading axis. A higher magnification view of the shear band is shown in Figure 17 showing the $170\ \mu\text{m}$ width of the band over which the localization occurs. Within the shear band, it is evident that the Saffil fibers have been broken into small pieces, as well as realigned along the direction of shear. The stark reorientation of the fibers at the boundary of the shear band is also apparent. We are in the process of making measurements of the distribution of fragment sizes; this in combination with the tensile strength of the fiber will permit estimating the effective length of the fibers as well as the quality of the processing.

A scanning electron micrograph of the failed specimen is shown in Figure 18. The bending and fracture process of the Saffil fibers as they get entrained into the shear localization is clearly identifiable in this image. Also, the nucleation and growth of microcracks at the boundary between the shear band and the unsheared region is evident; this apparently is the mechanism for the formation of the fractures that eventually separate the specimen into two pieces.

Similar tests have been performed under dynamic compression loading; the deformation and failure mechanisms are quite similar as described next.

3.2. Dynamic Compression Tests on Saffil-Fiber Filled MMC

The dynamic compression tests were performed on a Kolsky bar to attain strain rates around $2000\ \text{s}^{-1}$. The specimens had a rectangular cross-section ($9.6 \times 4.9\ \text{mm}$) and were observed with

high speed imaging throughout the tests. The images are used to identify when deformation becomes inhomogeneous, observe the failure process, and to measure the strain with DIC. Post-mortem microscopy was also performed to characterize the failure process better.

The dynamic compression responses from nine specimens corresponding to different compositions of Saffil content are shown in Figure 19. The measured stress strain curves are nearly identical to those found from quasi-static testing. These results indicate that the Saffil-Aluminum MMCs show no significant strain rate dependence in stress-strain behavior. Additionally, the Al-Cu matrix and composites with less than 30% volume fraction Saffil continue to increase their compressive load carrying capability for displacements in excess of 20% of the specimen's initial length. However, failure behavior for the 30% Saffil composite appears to be strongly dependent on strain rate.

Figure 20 shows the quasi-static and dynamic compressive structural responses for the 30% Saffil composite. Both the quasi-static and dynamic test specimens begin inhomogeneous deformation after a nominal strain of six percent. At this strain level a shear band forms as discussed in the previous section. At strains beyond the onset of shear band formation material constitutive behavior cannot be acquired, however observations about the structural response still prove useful. The quasi-static specimen unloads suddenly across a narrow range of compressive displacement shortly after the shear band forms. Conversely, the high strain rate specimen unloads very little over a large range of compressive displacement. Specimen displacement is measured both by analyzing the stress waves on the Kolsky bar and by performing DIC of the high speed camera images. The agreement between these independent measures is to within one and a half percent. Thus the dynamic compression specimen is able to dissipate significantly more energy than the quasi-static specimen.

The dynamic failure process observed from post-mortem microscopy follows the same overall progression as the quasi-static process. Regardless of strain rate, failure occurs through shear band localization followed by fracture in the localized region. Under quasi-static loading this is a well-organized process with a single band of highly deformed material growing into a single crack. The dynamic loading caused a dominant shear band, but with sporadic damage occurring on both of its flanks as shown in Figure 21. The patches of highly deformed material falling outside the main shear band appear to be the source of increased energy dissipation in

dynamically loaded specimens. Additionally, the dynamic compression specimen has much less fractured surface than the quasi-static specimen—even after enduring far more compression.

4. Behavior of Satin-Weave Nextel Fiber – MMC (DF-19)

Numerous specimens with different fiber architecture have been tested. In this report, we will limit attention to a 0/90 satin wave DF 19 under quasi-static compression and quasi-static tension loading. An optical microscope image of the typical microstructure of the satin weave DF-19 is shown in Figure 22. The material characterization tests were performed on specimens with a nominal rectangular cross-section (8×8 mm) at a strain rate in the range of 5.2×10^{-4} 1/s. Digital image correlation (DIC) was used to measure the strains and the load cell data was collected to estimate the stresses.

Under quasi-static tension, most of the DF-19 specimens failed with very little strain (less than 0.5%) regardless of the fiber architecture; the results from a number of these tension tests are shown in Figure 23. The only specimens that exhibited strains to about 5% were those that were tested in the matrix dominant direction. The fracture surface of one of the tensile specimens is shown in Figure 24. This image shows the different failure mechanisms that operate in this material. First, on the right hand side of the image, fracture of one tow of fibers that is aligned in the direction of the loading can be seen. The “pomegranate structure” where each fiber is surrounded by a sheath of the matrix is seen in this side; thus the matrix has infiltrated nearly perfectly into the interstices between the fibers. Second, the fibers that are either perpendicular to the loading direction or at a slight angle to it do not have to break; they simply debond along the fiber-matrix interface as can be seen in the mid region of Figure 24. Finally, the matrix-rich regions have to fail through plastic deformation and a ductile process of void nucleation and growth; this can be seen in the left hand side of Figure 24. Proper accounting for all of these modes of failure is essential in generating a failure model of the Nextel fiber reinforced MMC.

The quasi-static compressive response is shown in Figure 25. Once again, there is very little linear response in this material. The matrix inelasticity is transferred to the composite immediately; nevertheless, the strain hardening is significantly greater than in the matrix material. This is due to increased load sharing with the fiber-weave as well as possibly due to the smaller grain size that results from the numerous fiber-matrix interfaces that are generated during

fabrication of the composite. Additional microscopy and modeling efforts are needed to quantify these two effects. Furthermore, the unloading response indicated significant Bauschinger effect. All of the compression specimens failed due to a matrix dominated shear localization. This is illustrated in Figure 26, where an optical microscope image of a polished section is shown. The two red lines indicate the boundaries of the shear band and demonstrate that this occurs at an angle of 54° with respect to the loading axis, suggesting a uniaxial stress state. A higher magnification view of the shear band is shown in Figure 27 showing the $170\ \mu\text{m}$ width of the band over which the localization occurs. Within the shear band, it is evident that the Nextel fibers have been broken into small pieces, as well as realigned along the direction of shear. The stark reorientation of the fibers is evident at the boundary of the shear band is also apparent. Figure 28 shows a scanning electron micrograph of a region in the vicinity of the boundary of the shear band; fragmentation of the fiber and the formation and linking of fine cracks in the matrix are also visible in this figure. To quantify these failure processes a modeling effort that incorporates these mechanisms in a unit cell model is needed.

5. Summary and Conclusions

The quasi-static and dynamic response of metal matrix composites have been examined. Three different types of materials were examined: unidirectionally reinforced continuous fiber $\text{Al}_2\text{O}_3/\text{Al}$ metal matrix composite, random fiber Saffil-fiber – aluminum matrix composite, and a satin-weave Nextel fiber reinforced aluminum matrix composite. Standard quasi-static tests and specially designed dynamic tests using a standard split-Hopkinson pressure bar apparatus have been performed. For the split-Hopkinson bar test, in addition to the conventional measurements of the strain signals in the input and output bars, direct images of the deformation of the specimen were obtained using a Photron SA1 high speed video camera at $10\ \mu\text{s}$ time intervals. These measurements indicated that while the stress on either side of the specimen attained the same value assuring stress uniformity along the length of the specimen, the deformation was localized due to the formation and propagation of a kink band. Based on an analysis of the power balance in the specimen, the rate of dissipation at the propagating kink band was estimated and used subsequently to determine that the dynamic dissipation was significantly greater than the

quasi-static dissipation in the same material. The underlying reason was explored through a microscopic examination and attributed to increased fiber breakage under dynamic loading conditions.

This report also documents some of the highlights of the material response of Saffil filled aluminum matrix composite and a Nextel satin weave reinforced aluminum matrix composite. As indicated, while the matrix is very soft with a low yield stress, the random or woven fiber reinforcement brings about significant stiffening of the material. The modulus increase follows roughly the rule of mixtures, with exceptions occurring due to the presence of defects in fiber distribution within the matrix. The plastic flow properties are enhanced significantly by the addition of the fibers; with 30% fiber fraction, the yield stress increases by a factor of 20 and the flow stress by about a factor of 5. The deformation mechanisms appear to rely on the rotation and breaking of the fibers to accommodate the flow of the matrix. Final failure occurs through the formation of a shear band, just as in the case of the matrix, although at significantly greater stress and deformation levels.

REFERENCES

- Argon AS, 1972, Fracture of composites, *Treatise of Materials Science and Technology*, Vol. 1., Academic Press, New York.
- Argon AS, 2000, Fracture: Stength and Toughness Mechanisms, in **Comprehensive Composite Materials**, Volume 1, Elsevier, 763-802
- Budiansky B; Fleck NA, 1993, Compressive failure of fibre composites, *Journal of the Mechanics and Physics of Solids*, **41**, 183-211.
- Chin ESC, 1999, Army focused research team on functionally graded armor composites, *Materials Science and Engineering A*, **259**, 155-161.
- Chu TC; Ranson WF; Sutton MA; Peters WH, 1985, Applications of digital-image correlation techniques to experimental mechanics, *Experimental Mechanics*, **25**, 232-244.
- Cox HL, 1952, The elasticity and strength of paper and other fibrous materials, *British Journal of Applied Physics*, **3**, 72-79.
- Dai LH; Bai YL, 1998, Transverse shear strength of unidirectional carbon fiber reinforced aluminum matrix composite under static and dynamic loadings, *Journal of Composite Materials*, **31**, 246-257.
- Deve HE; McCullough C, 1995, Continuous-fiber reinforced Al composites: A new generation, *Journal of Metals*, **47**, 33.
- Eshelby JD, 1957, The determination of the elastic field of an ellipsoidal inclusion, and related problems, *Proceedings of the Royal Society of London A*, **241**, 376-396.
- Hershey AV, 1954, The elasticity of an isotropic aggregate of an anisotropic cubic crystals, *Journal of Applied Mechanics*, **21**, 236-240.
- Ibrahim IA; Mohamed FA; Lavernia EJ, 1991 Particulate reinforced metal matrix composites – A review, *Journal of Materials Science*, **26**, 1137-1156.
- Jones RM, 1975, *Mechanics of Composite Materials*, McGraw-Hill.
- Kiser MT; Zok FW; Wilkinson DS, 1996, Plastic flow and fracture of a particulate metal matrix composite, *Acta Materialia*, **44**, 3465-3476.
- Kyriakides S; Arsecularatne R; Perry EJ; Liechti KM, 1995 On the compressive failure of fiber reinforced composites, *International Journal of Solids and Structures*, **32**, 689-738.

Lee WS; Sue WC; Chiou ST, 2000, Effect of reinforcement orientation on the impact fracture of carbon fiber reinforced 7075-T6 aluminum matrix composite, *Materials Transactions, Japan Institute of Metals*, **41**, 1055-1063.

Lloyd DJ, 1994 Particle-reinforced aluminum and magnesium matrix composites, *International Materials Reviews*, **39**, 1-23.

Luo A, 1995 Processing, microstructure, and mechanical-behavior of cast magnesium metal matrix composites, *Metallurgy and Materials Science*, **26**, 2445-2455.

Rosen BW, 1965, Mechanics of composite strengthening, *Fiber Composite Materials*, Seminar of the American Society for Metals, p.37-75.

Saravanan RA; Surappa MK, 2000, Fabrication and characterization of pure magnesium-30 vol.% SiC_p particle composites, *Materials Science and Engineering A*, **276**, 108-116.

Shetty HR; Chou T-W, 1985, Mechanical properties and failure characteristics of FP/aluminum and W/aluminum composites, *Metallurgical Transactions A*, **16A**, 853-864.

Totry E; González C; LLorca J, 2008, Failure locus of fiber-reinforced composites under transverse compression and out-of-plane shear, *Composites Science and Technology*, **68**, 829-839.

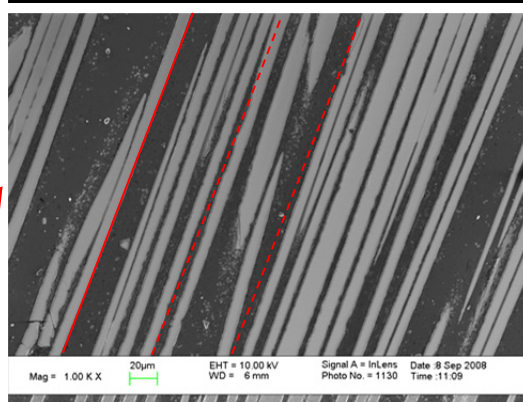
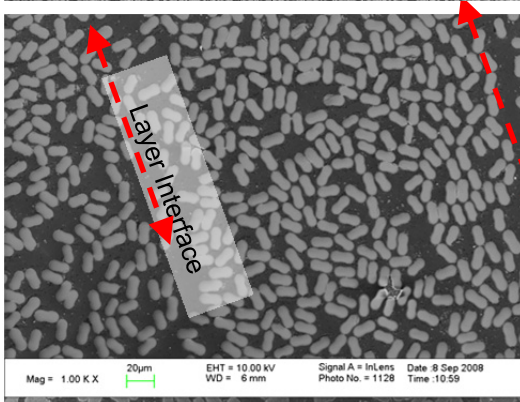
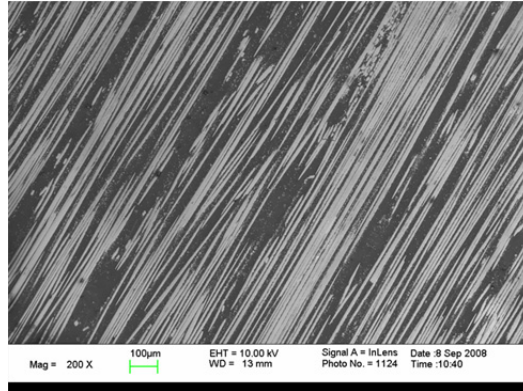
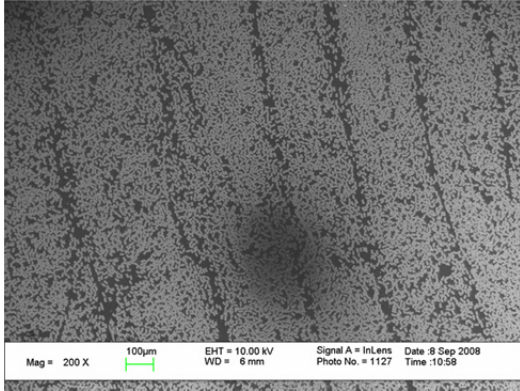
Vogler TJ; Kyriakides S, 1999, On the axial propagation of kink bands in fiber composites: Part I: Experiments, *International Journal of Solids Structures*, **36**, 557.

Voigt W, 1889, Über die beziehung zwischen den beiden elasticitats-constanten isotroper korper, *Wied Ann Physik*, **38**, 573-587.

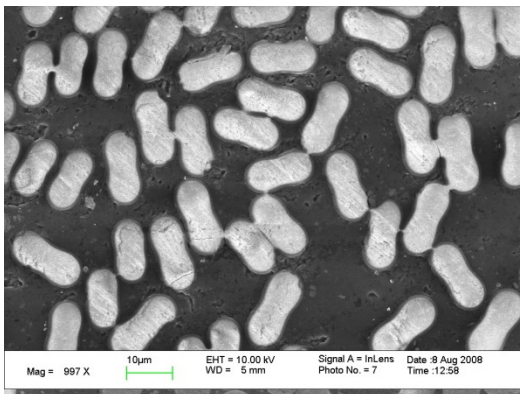
Yadav S; Chichili DR; Ramesh KT, 1995, The mechanical response of A 6061-T6 Al/Al₂O₃ metal matrix composite at high rates of deformation, *Acta Metallurgica et Materialia*, **43**, 4453-4464.

Zhang H; Chen MW; Ramesh KT; Ye J; Schoenung JM, 2006, Tensile behavior and dynamic failure of aluminum 6092/B₄C composites, *Materials Science and Engineering A*, **433**, 70-82.

Zhang H; Ramesh KT; Chin ESC, 2008 A multi-axial constitutive model for metal matrix composites, *Journal of the Mechanics and Physics of Solids*, **56**, 2972-2983.

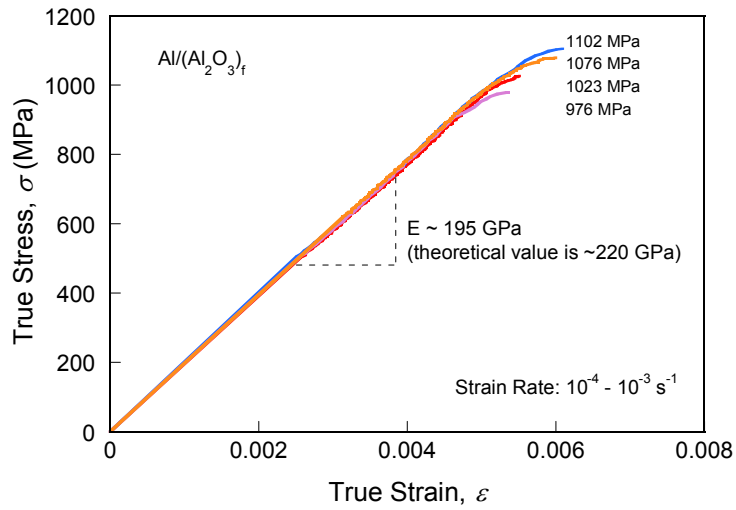


(b) Axial Plane

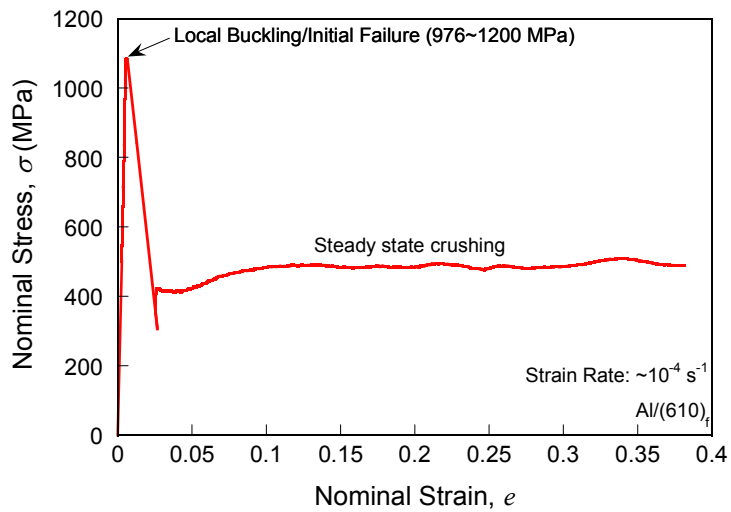


(a) Transverse Plane

Figure 1. Microstructure of the Nextel 610 Al composite. (a) Transverse section indicating matrix rich layers and a high magnification of the transverse section indicating the peanut shape cross-section: $\sim 16 \times 8 \mu\text{m}$; (b) Axial section indicating the nominal orientation of the unidirectional fibers and some misaligned fibers. The red solid line is the nominal fiber direction, while the red dashed lines are parallel to the fiber direction and indicate the degree of misalignment.



(a)



(b)

Figure 2. (a) True stress vs true strain variation for the elastic portion of the response. (b) Nominal stress vs nominal strain response of the specimen that covers initiation of the kink band as well as the steady state crushing of the specimen.

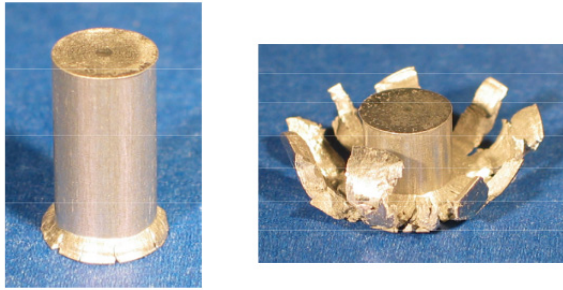


Figure 3. (a) Photograph of a specimen that was unloaded just past the initiation of the kink band localization. (b) Specimen that was crushed through nearly half of its initial length; petaling type of failure is observed (Video file of the development of this kind of failure is available as supplementary material to this article).

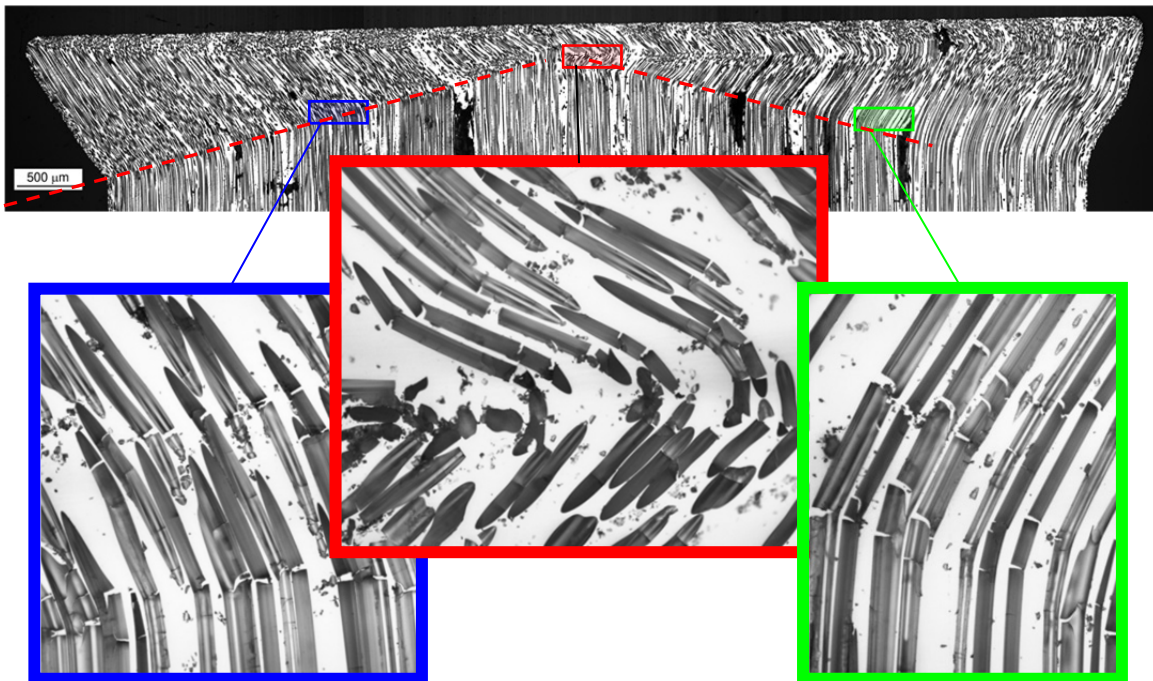


Figure 4. An axial section of the specimen interrupted just past the initiation of the kink band is shown. The red dashed lines indicate the orientation of the kink band, which is $\sim 15^\circ$ with respect to the loading axis. High magnification images of the regions at the band ends indicate bending and fracture of the fibers. At the central region, the intersection of bands oriented along two equivalent planes result in significant fragmentation of the fibers.

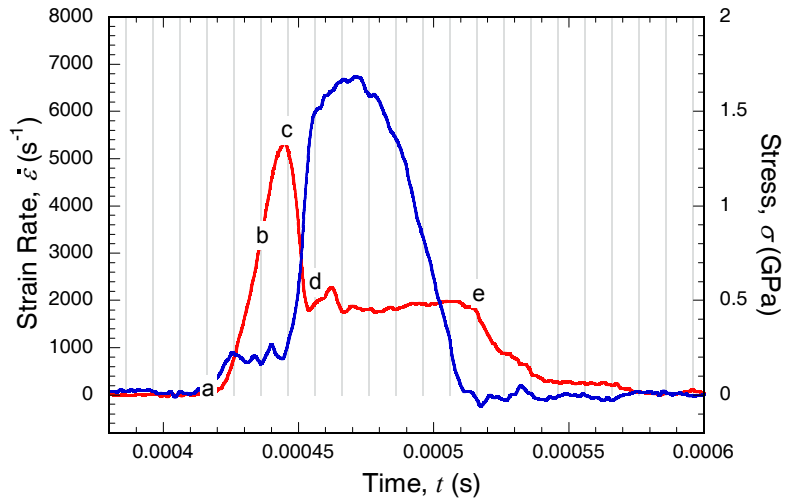


Figure 5. Time variation of the reflected signal in the input bar converted the nominal strain rate in the specimen (blue line) and the transmitted signal in the output bar converted to the stress in the specimen (red line). The gray vertical lines indicate times at which high speed video images were recorded. Labels (a) through (e) identify the times corresponding to times for which images are shown in Figure 6.

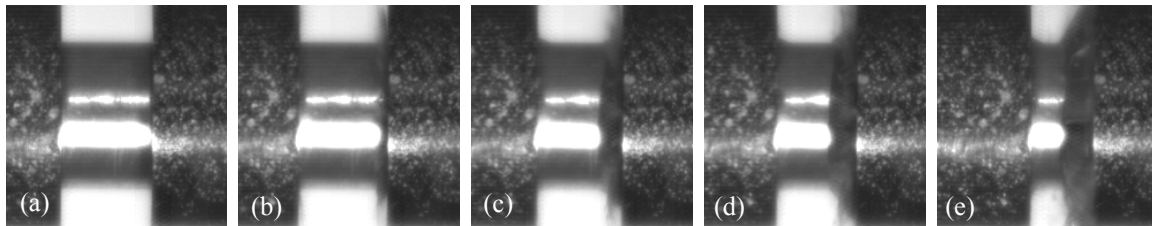


Figure 6. Selected frames from the high speed video sequence of one test indicating the uniform strain development up to frame (c) and kink band propagation from stage (d). The complete movie is available online as Supplementary Material.

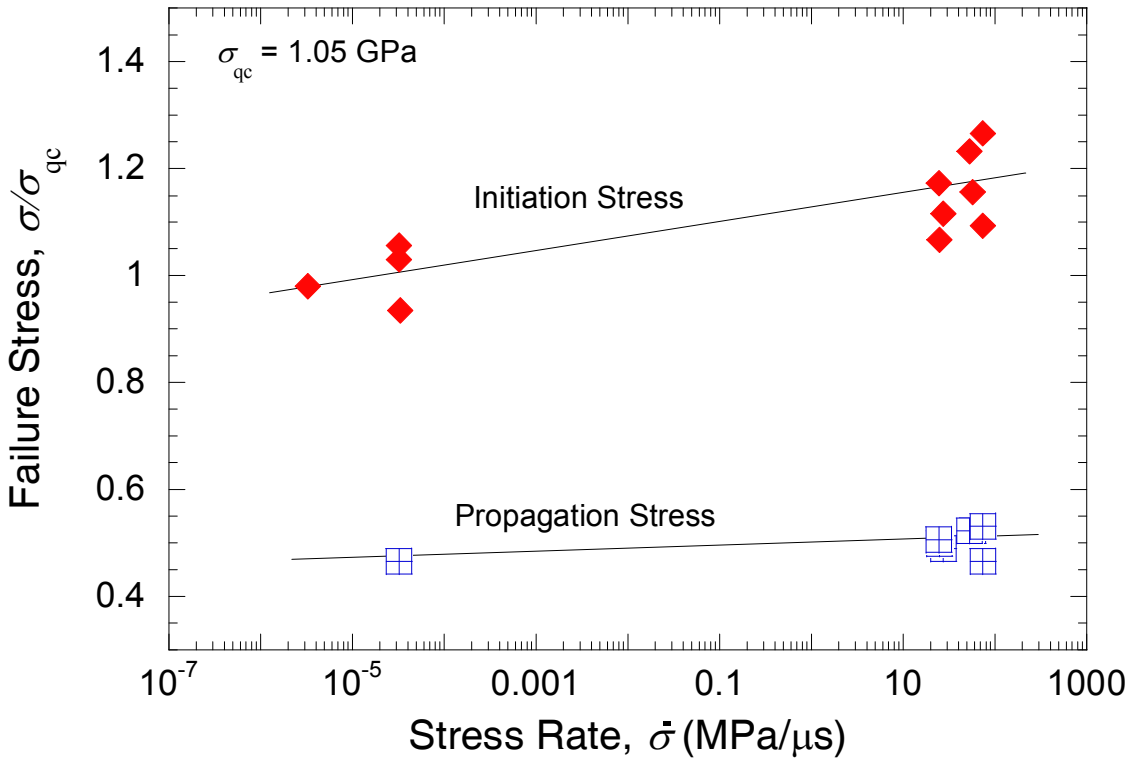


Figure 7. Variation of the kink initiation and propagation stress with loading rate.

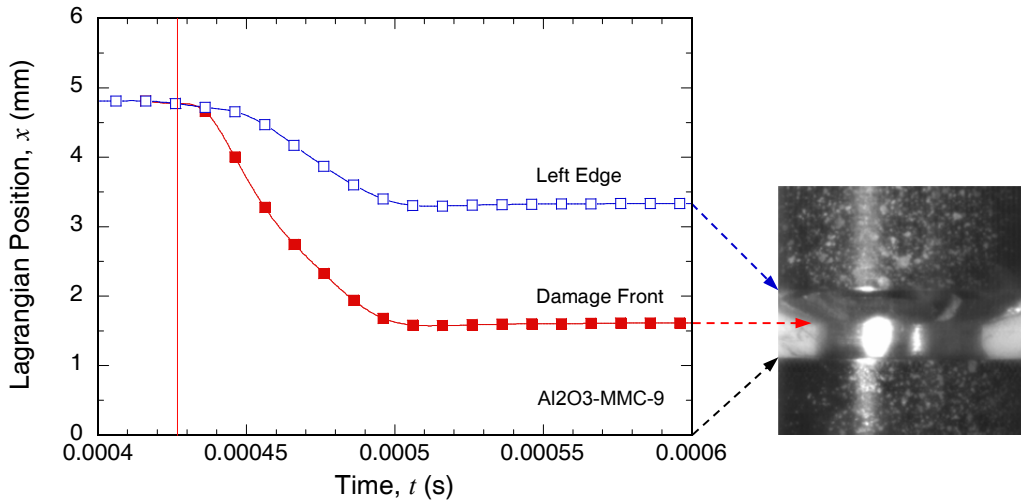


Figure 8. The time variation of the position of the left edge of the specimen and the position of the kink band (labeled damage front) with reference to the right edge of the specimen.

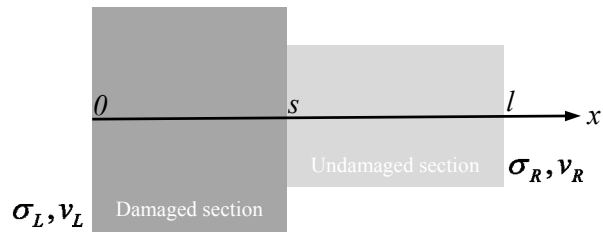


Figure 9. Geometry of the specimen indicating the nonuniform strain distribution. The input and output bars are in contact with the specimen at $x = 0$ and $x = l$, respectively. The kink band is at $x = s(t)$.

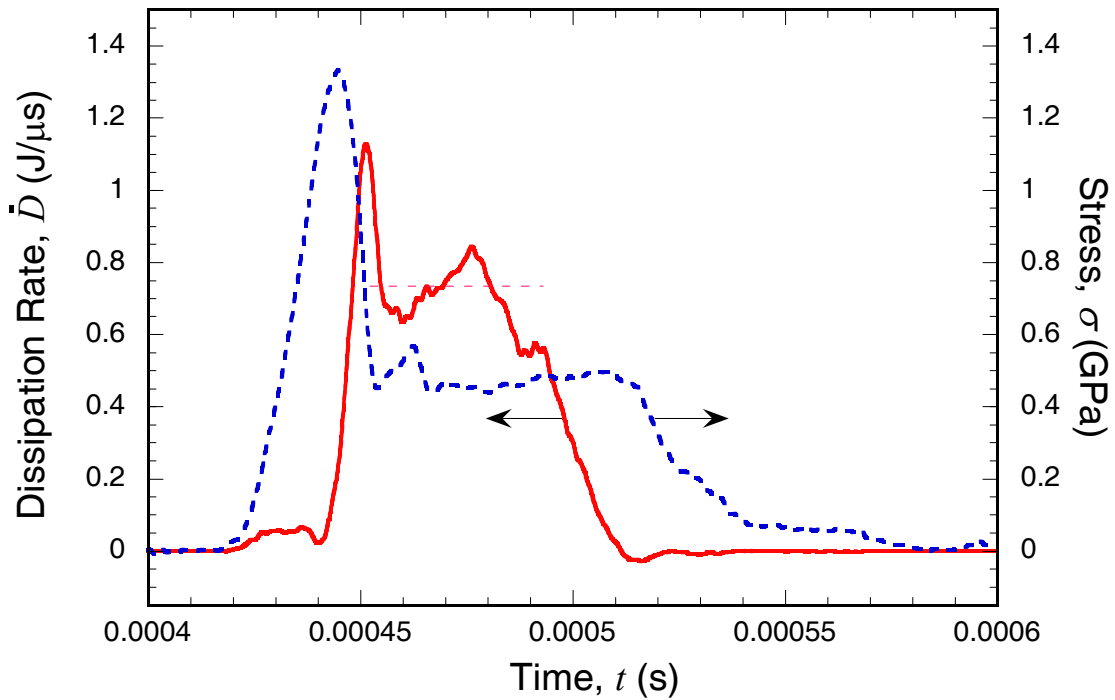


Figure 10. Time variation of the dissipation rate, \dot{D} (solid red line), and the stress in the specimen (blue dashed line).

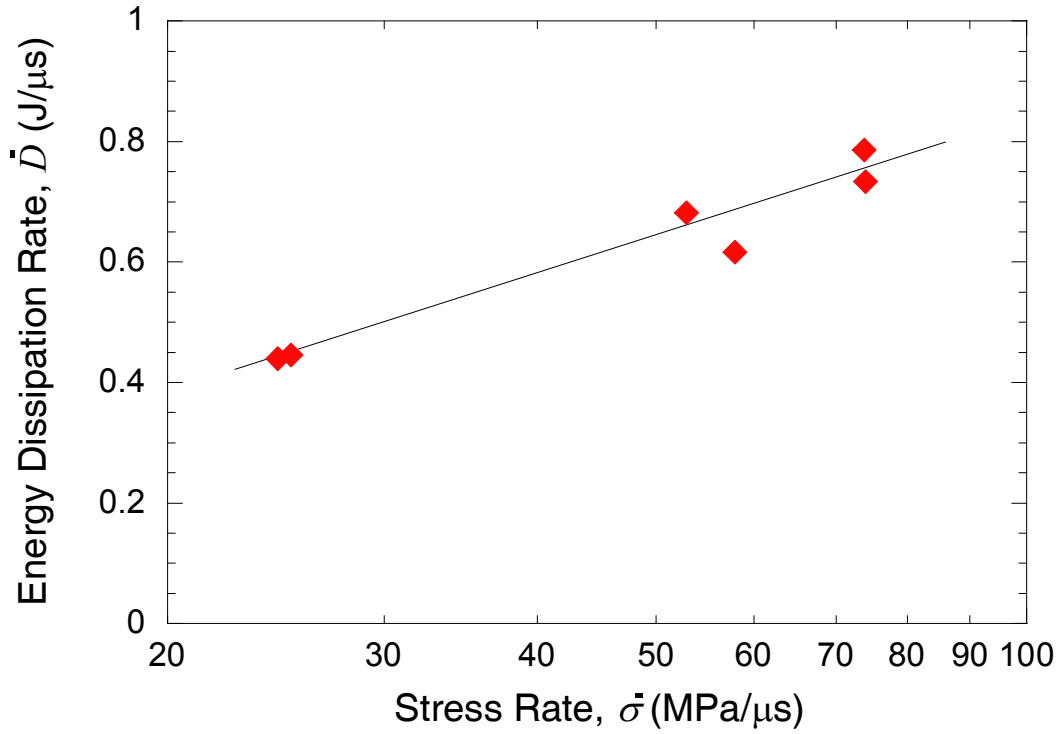


Figure 11. Variation of the dissipation rate with the loading rate.

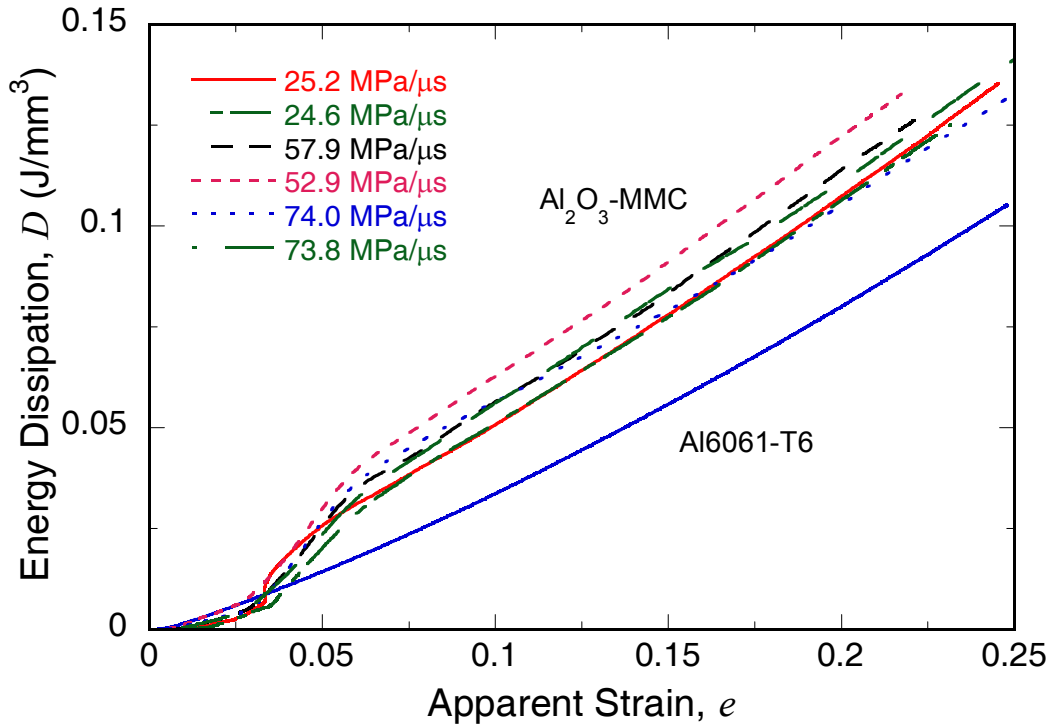


Figure 12. Loading rate dependence of dissipation during kink band propagation.

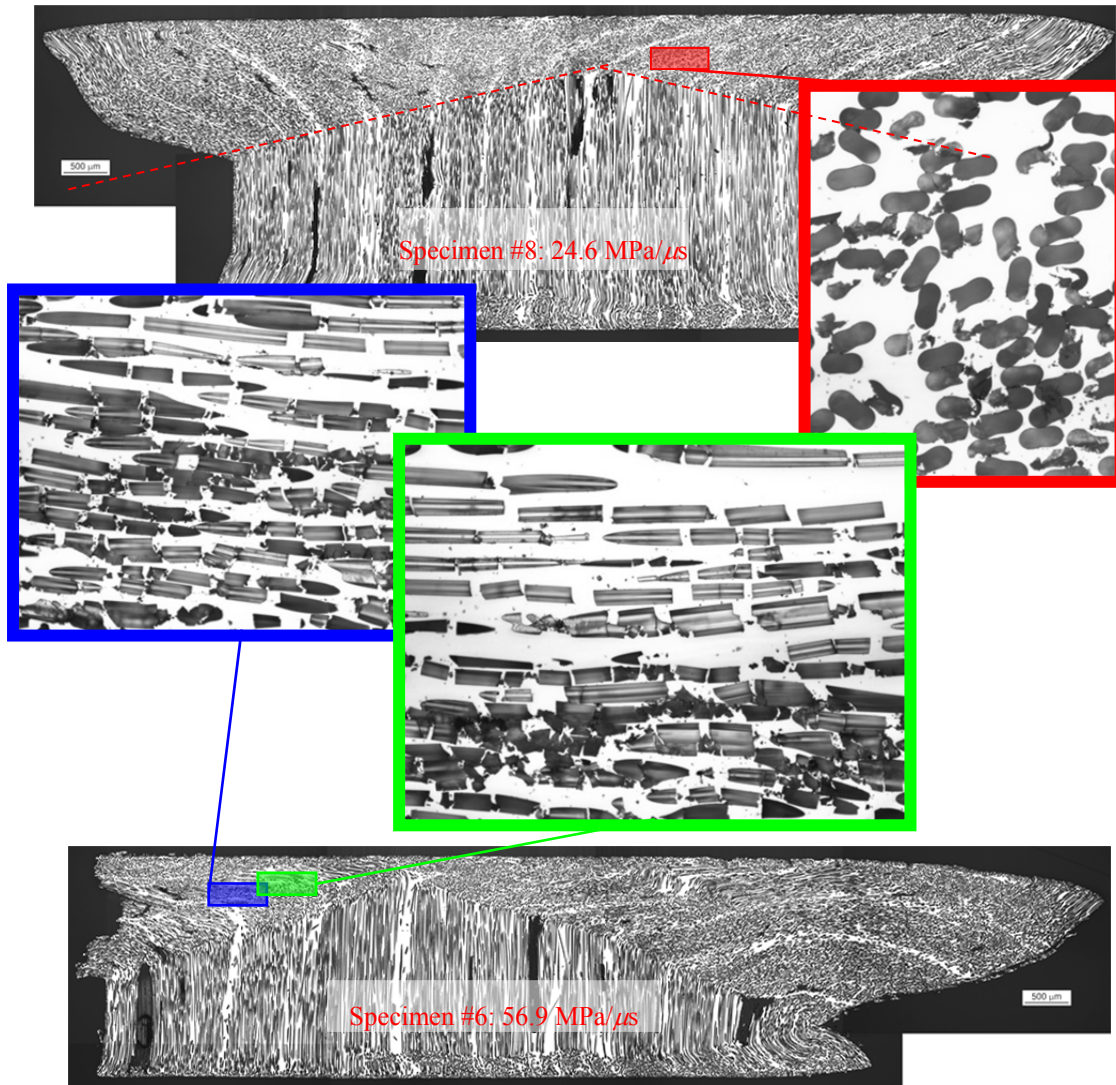


Figure 13. Axial sections of two specimens, at loading rates $\dot{\sigma} = 24.6$ and $\dot{\sigma} = 54.9$ MPa/ μ s respectively, in the top and bottom images, indicating the kink band progression. The red dashed lines indicate the orientation of the kink band, which is $\sim 15^\circ$ with respect to the loading axis, similar to that in the quasi-static kink propagation. High magnification images of the regions at the band ends indicate bending and fracture of the fibers. The main difference from quasi-static band propagation appears to be in the increased number of fragments in the dynamic experiments.

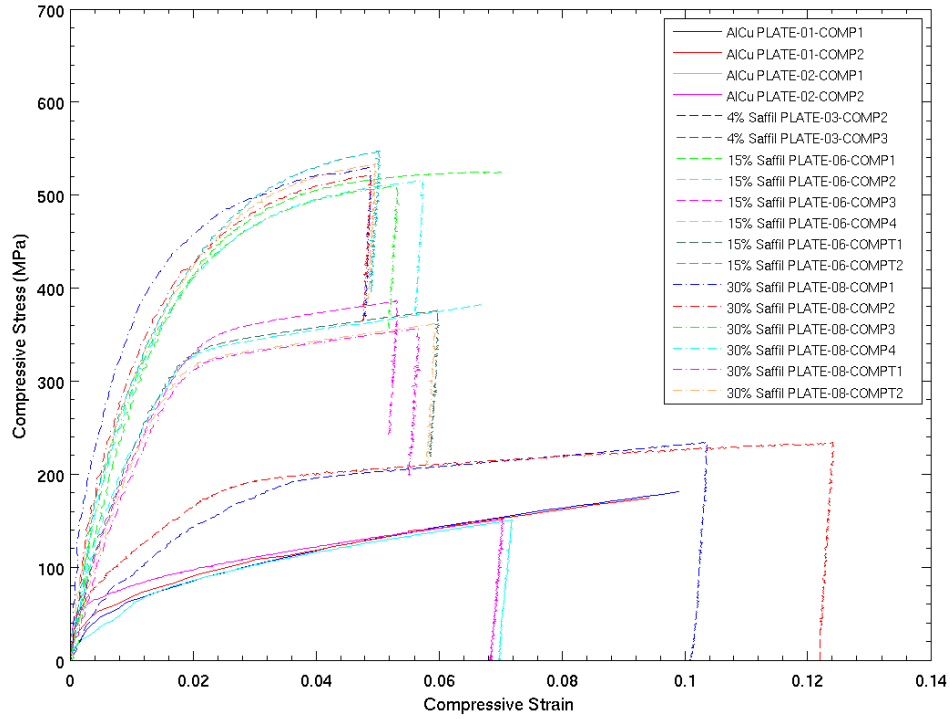


Figure 14. Quasi-static compression response of Saffil fiber aluminum matrix composites. Matrix response indicates a very small initial yield strength.

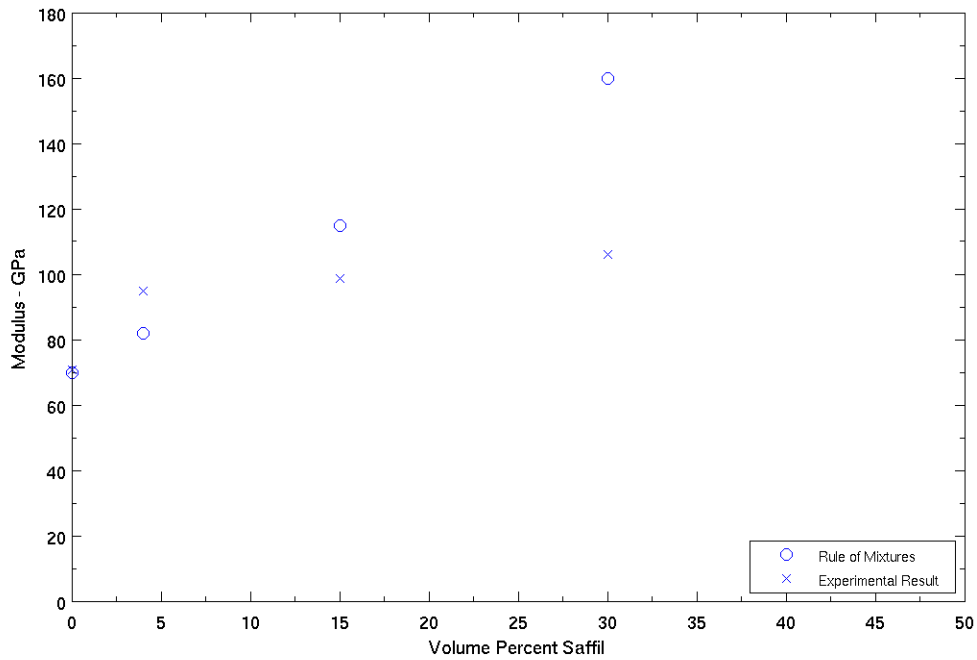


Figure 15. Elastic modulus of Saffil fiber aluminum matrix composites, obtained from the unloading segments in Figure 1. The estimate from the rule of mixtures is indicated by the open circular symbols.

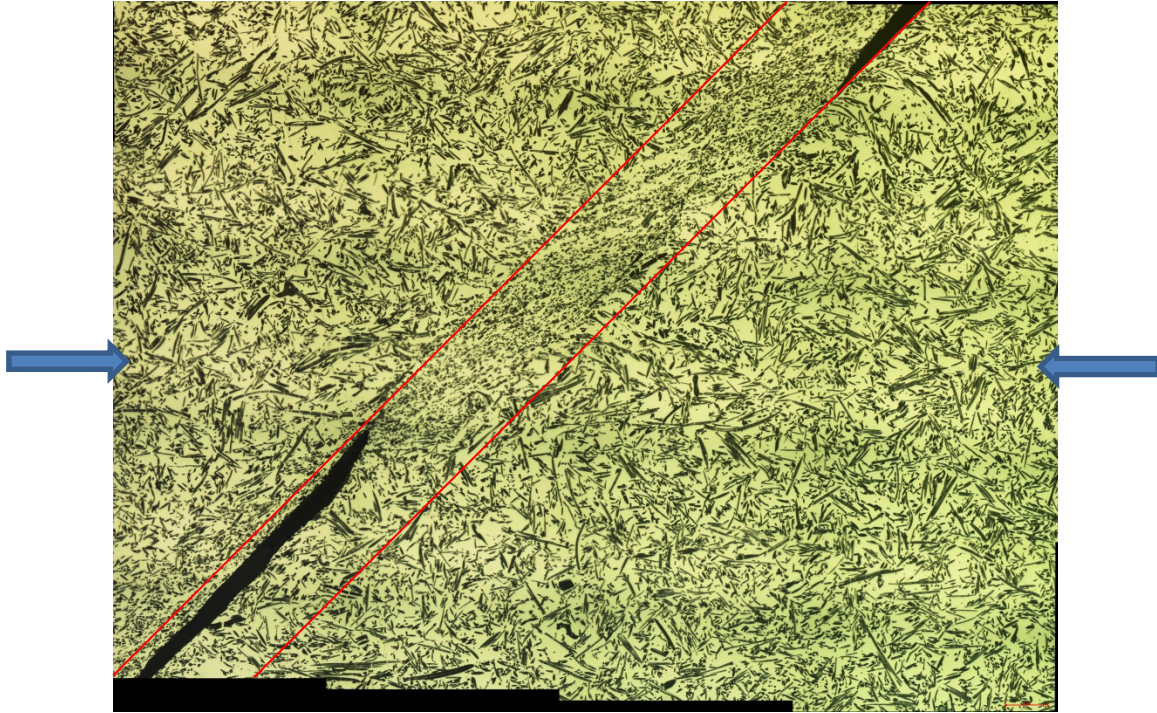


Figure 16. Shear localization and failure response of Saffil fiber aluminum matrix composites (15% Saffil. Al2%Cu Matrix). Cracks have appeared, typically in the boundary of the shear band.



Figure 17. Close up view of the shear localization in Figure 16. (15% Saffil)

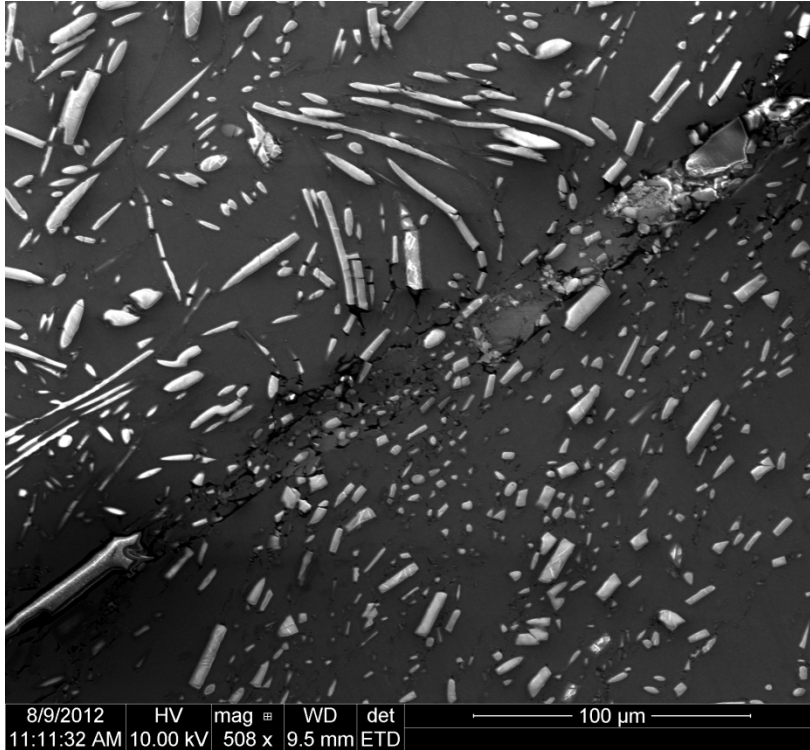


Figure 18. Scanning electron micrograph of the 15% Saffil in the region of the shear band. Matrix damage and microcracks appear over a much smaller portion of the shear band (over 10 μm near one boundary).

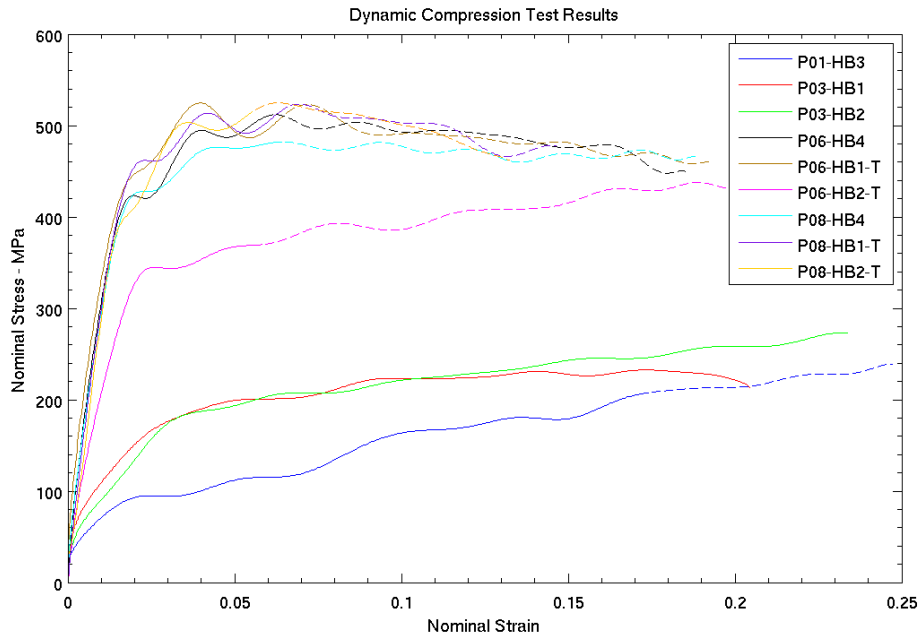


Figure 19. Dashed lines show specimen response after inhomogenous deformation begins. P03 specimens were not recorded with high speed imaging so the boundary between material and structural response is unknown.

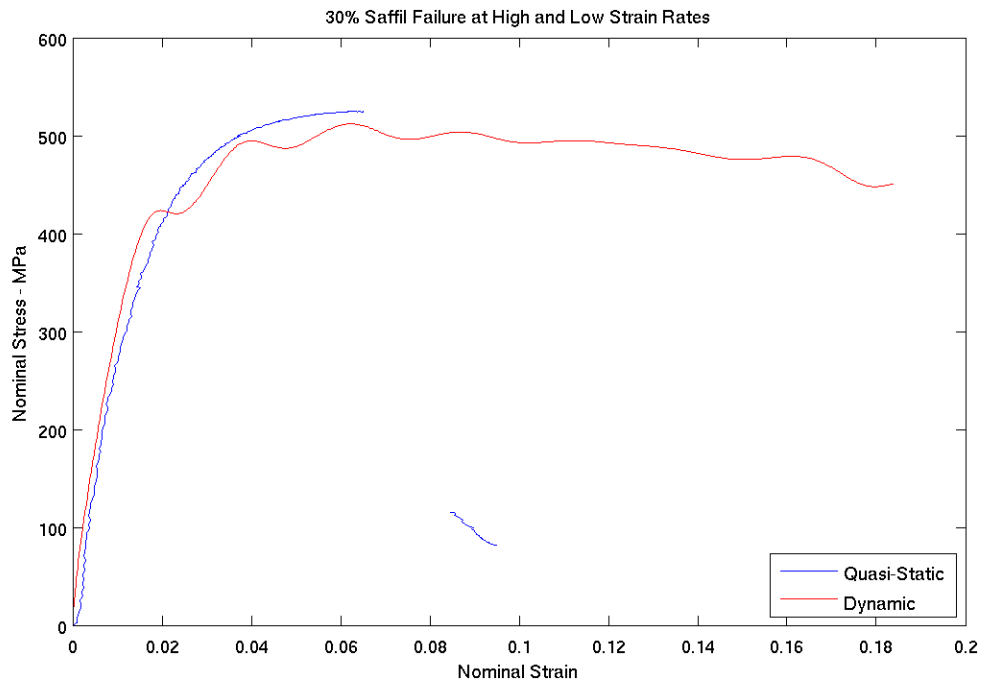


Figure 20. The dependency of load carrying response in the damaging regime on strain rate is large. The separation between the two blue curves is caused from the interaction between the specimen and loading frame during specimen fracture.



Figure 21. Optical micrograph of 30% Saffil composite after dynamic compression. Damage is visible outside the dominant band.

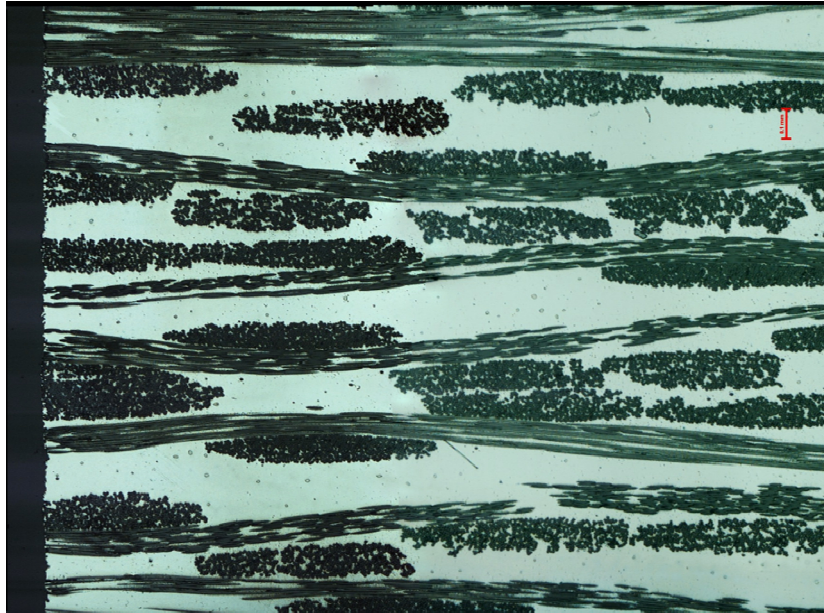


Figure 22. Optical micrograph of the satin-weave Nextel – Aluminum matrix composite.

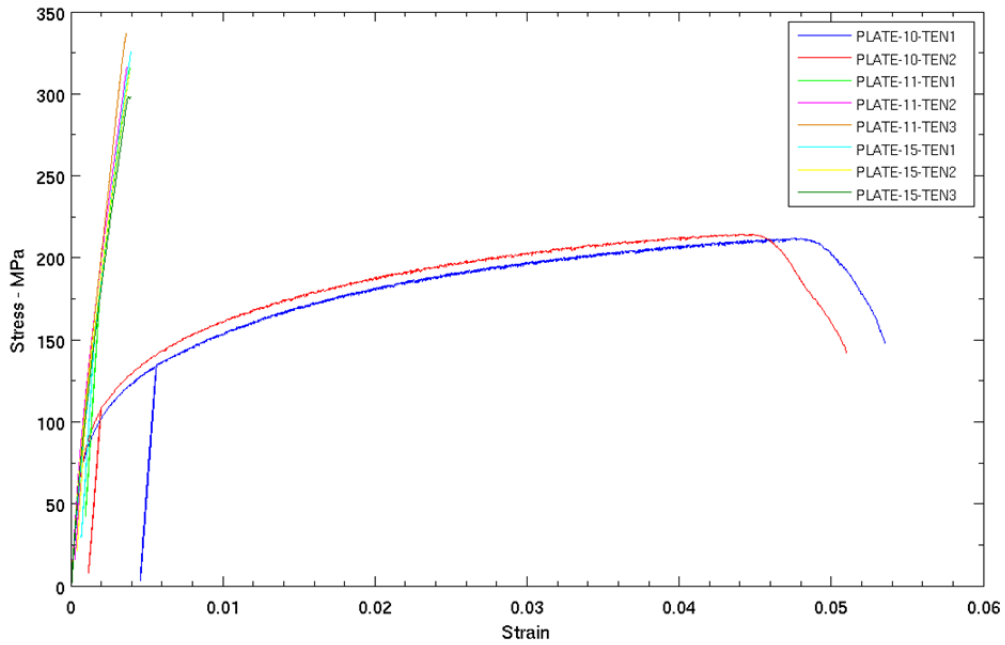


Figure 23. Tensile stress-strain response of DF-19 (0/90 satin weave Nextel-aluminum matrix composite). The only material to exhibit a ductile response was tested in the matrix dominant direction (perpendicular to the fibers).

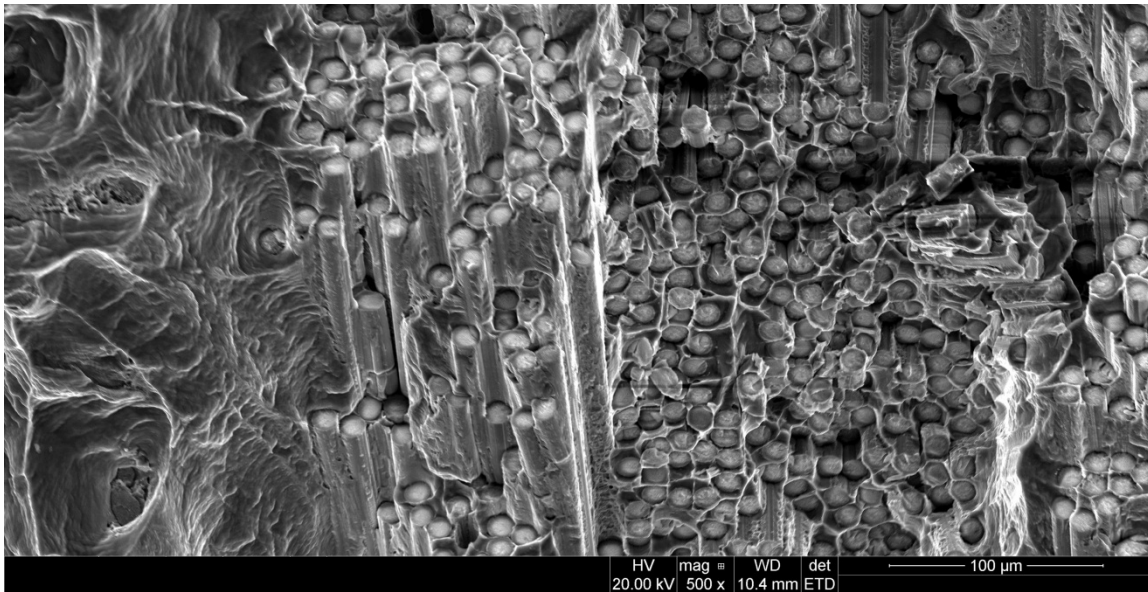


Figure 24. Fracture surface of a broken DF-19 satin-weave (0/90) Nextel-fiber aluminum matrix composite. The complete infiltration of the metal inside the fiber tows can be seen in this micrograph.

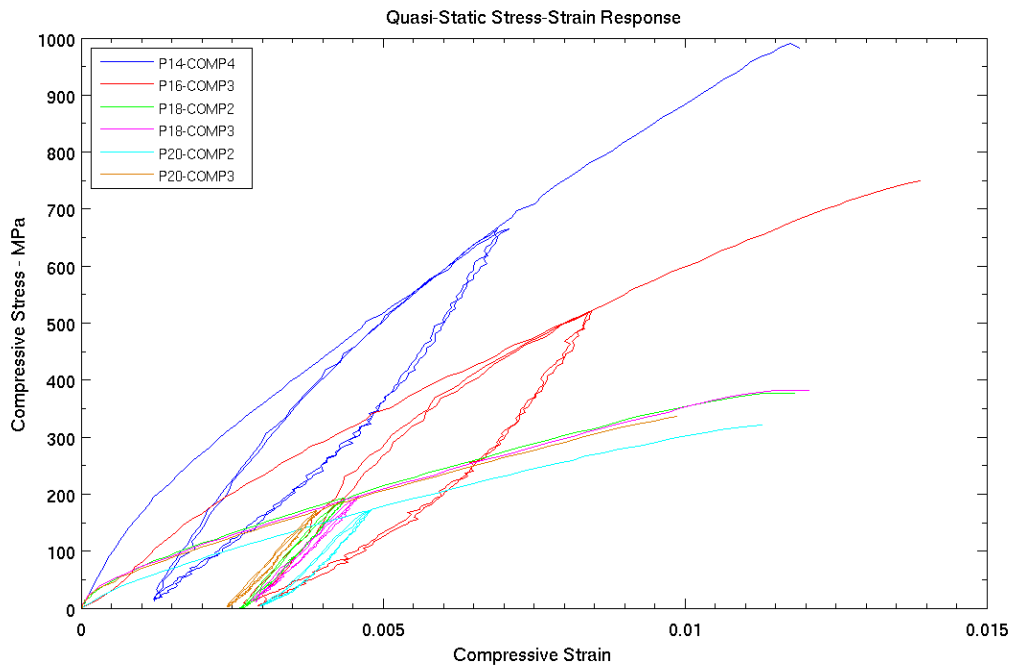


Figure 25. Quasi-static compression response of Nextel fiber aluminum matrix DF-19 composites. Matrix response indicates a very small yield strength as shown in Figure 1.

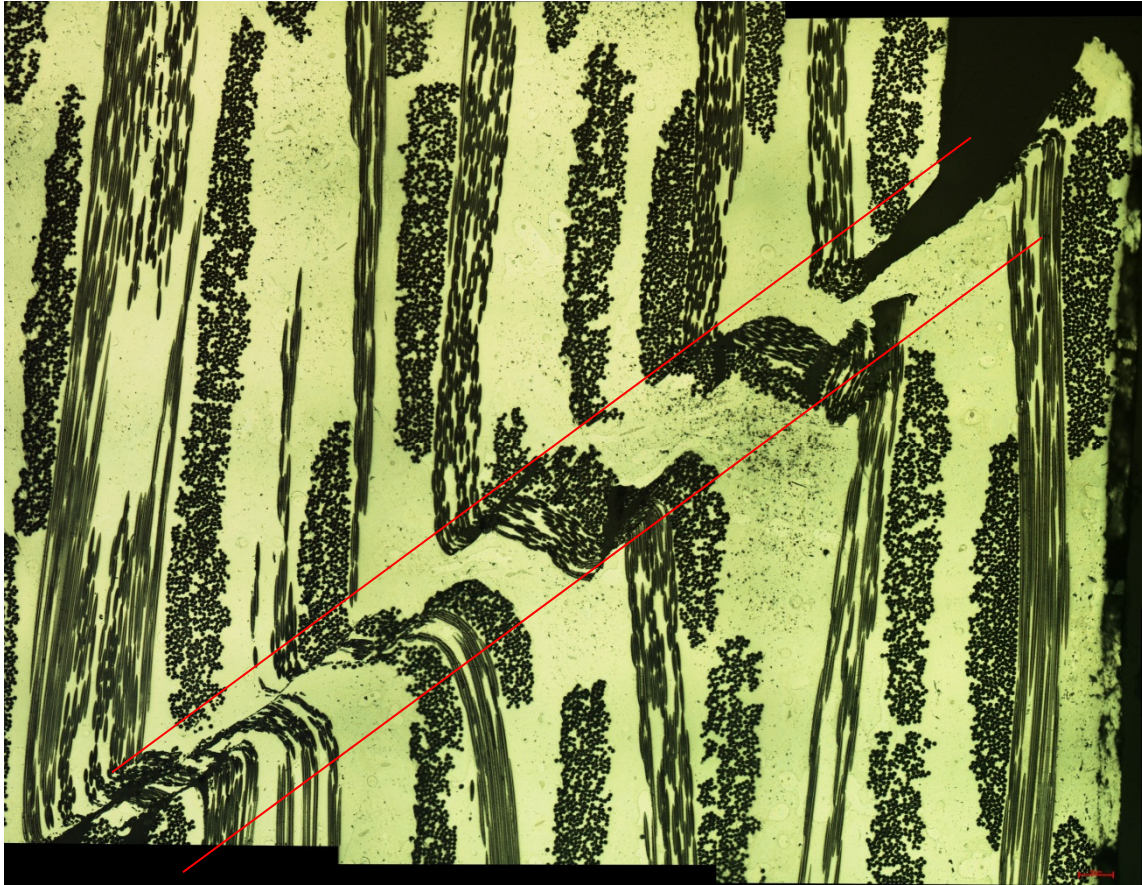


Figure 26. Shear localization and kinks in the fiber. Nextel-aluminum matrix DF-19 specimen under compression. The shear band makes an angle of 54° with respect to the loading axis.

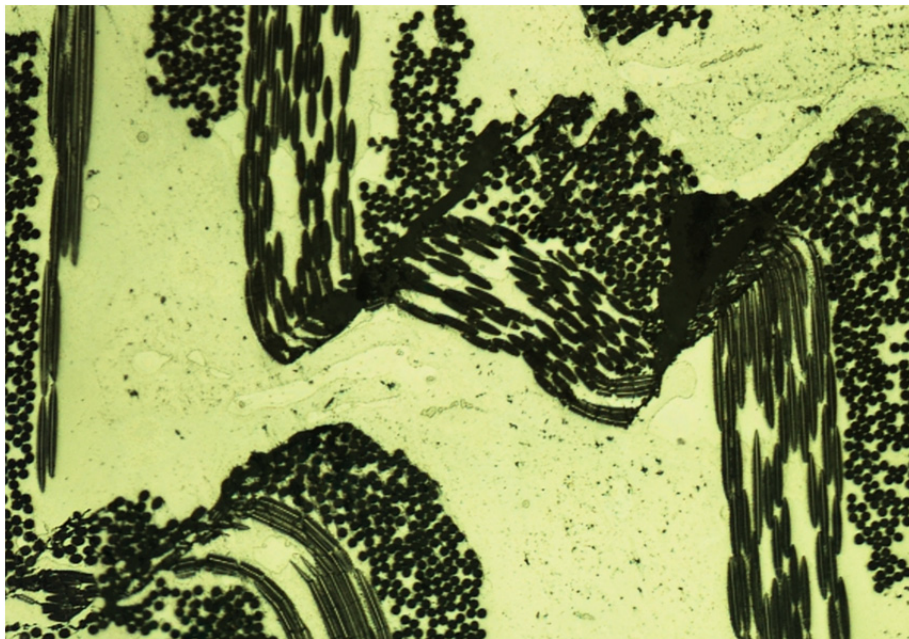


Figure 27. Close up view of the shear localization and kinks in Figure 26.

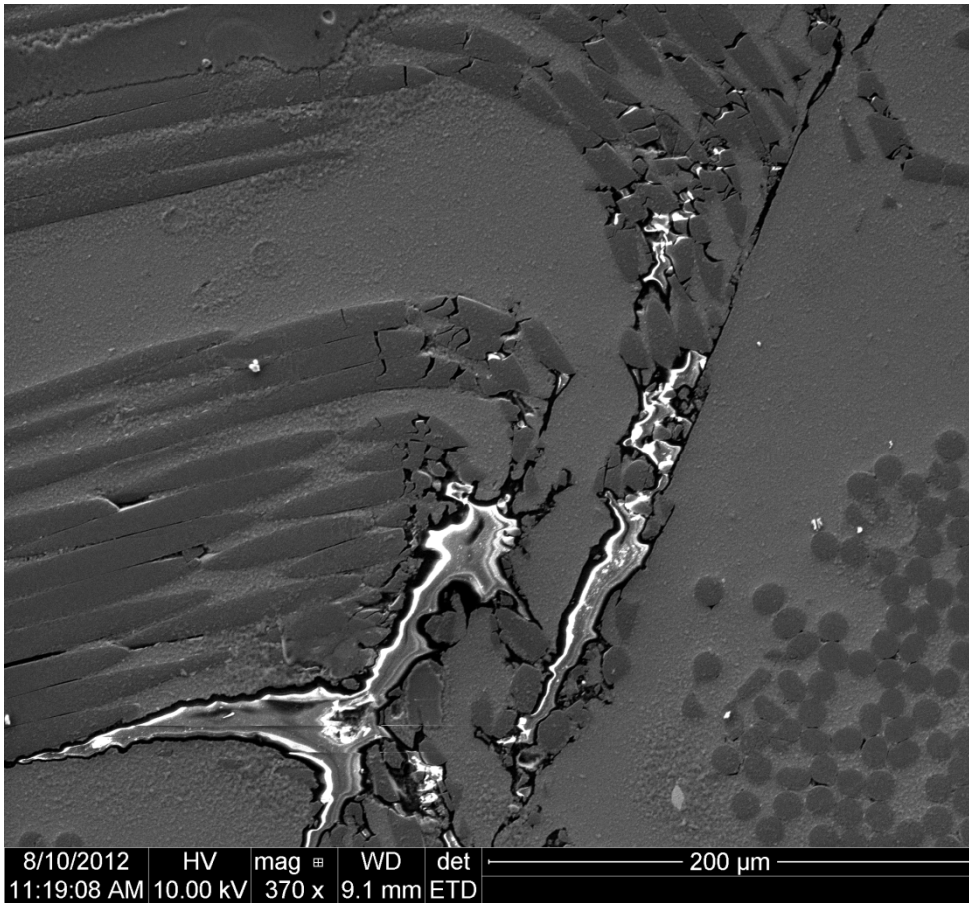


Figure 28. Scanning electron microscope image of the boundary of the shear band indicating large fiber rotation, fiber fracture and matrix cracking.